

# Aseismic Fault Slip during a Shallow Normal-Faulting Seismic Swarm Constrained Using a Physically-Informed Geodetic Inversion Method

Yu Jiang<sup>1</sup>, Sergey Samsonov<sup>2,2,2</sup>, Pablo J González<sup>1,1,1</sup>, and Yu Jiang<sup>1,1</sup>

<sup>1</sup>University of Liverpool

<sup>2</sup>Natural Resources Canada

December 1, 2022

## Abstract

Improved imaging of the spatio-temporal growth of fault slip is crucial for understanding the driving mechanisms of earthquakes and faulting. This is especially critical to properly evaluate the evolution of seismic swarms and earthquake precursory phenomena. Fault slip inversion is an ill-posed problem and hence regularisation is required to obtain stable and interpretable solutions. An analysis of compiled finite fault slip models shows that slip distributions can be approximated with a generic elliptical shape, particularly well for  $M[?]7.5$  events. Therefore, we introduce a new physically-informed regularisation to constrain the spatial pattern of slip distribution. Our approach adapts a crack model derived from mechanical laboratory experiments and allows for complex slipping patterns by stacking multiple cracks. The new inversion method successfully recovered different simulated time-dependent patterns of slip propagation, i.e., crack-like and pulse-like ruptures, directly using wrapped satellite radar interferometry (InSAR) phase observations. We find that the new method reduces model parameter space, and favours simpler interpretable spatio-temporal fault slip distributions. We apply the proposed method to the 2011 March-September normal-faulting seismic swarm at Hawthorne (Nevada, USA), by computing ENVISAT and RADARSAT-2 interferograms to estimate the spatio-temporal evolution of fault slip distribution. The results show that (1) aseismic slip might play a significant role during the initial stage, and (2) this shallow seismic swarm had slip rates consistent with those of slow earthquake processes. The proposed method will be useful in retrieving time-dependent fault slip evolution and is expected to be widely applicable to studying fault mechanics, particularly in slow earthquakes.

# Aseismic Fault Slip during a Shallow Normal-Faulting Seismic Swarm Constrained Using a Physically-Informed Geodetic Inversion Method

Yu Jiang<sup>1</sup>, Sergey V. Samsonov<sup>2</sup>, and Pablo J. González<sup>1,3</sup>

<sup>1</sup>COMET, Dept. Earth, Ocean and Ecological Sciences, School of Environmental Sciences, University of  
Liverpool, Liverpool, L69 3BX, United Kingdom.

<sup>2</sup>Canada centre for Mapping and Earth Observation, Natural Resources Canada, 560 Rochester Street,  
Ottawa, ON K1S5K2, Canada.

<sup>3</sup>Department of Life and Earth Sciences, Instituto de Productos Naturales y Agrobiología (IPNA-CSIC),  
38206 La Laguna, Tenerife, Canary Islands, Spain.

## Key Points:

- We invert for time-dependent fault slip distribution from geodetic data, based on a low dimensional model for elliptical slip distributions.
- Significant aseismic slip preceded the most energetic M4.6 event in the 2011 Hawthorne shallow seismic swarm.
- Average slip rates (lower bound) of this swarm and slow-slip phenomena are similar, implying a notable role of aseismic processes in swarms.

---

Corresponding author: Yu Jiang, [jiangyuinsar@gmail.com](mailto:jiangyuinsar@gmail.com)

## Abstract

Improved imaging of the spatio-temporal growth of fault slip is crucial for understanding the driving mechanisms of earthquakes and faulting. This is especially critical to properly evaluate the evolution of seismic swarms and earthquake precursory phenomena. Fault slip inversion is an ill-posed problem and hence regularisation is required to obtain stable and interpretable solutions. An analysis of compiled finite fault slip models shows that slip distributions can be approximated with a generic elliptical shape, particularly well for  $M \leq 7.5$  events. Therefore, we introduce a new physically-informed regularisation to constrain the spatial pattern of slip distribution. Our approach adapts a crack model derived from mechanical laboratory experiments and allows for complex slipping patterns by stacking multiple cracks. The new inversion method successfully recovered different simulated time-dependent patterns of slip propagation, i.e., crack-like and pulse-like ruptures, directly using wrapped satellite radar interferometry (InSAR) phase observations. We find that the new method reduces model parameter space, and favours simpler interpretable spatio-temporal fault slip distributions. We apply the proposed method to the 2011 March-September normal-faulting seismic swarm at Hawthorne (Nevada, USA), by computing ENVISAT and RADARSAT-2 interferograms to estimate the spatio-temporal evolution of fault slip distribution. The results show that (1) aseismic slip might play a significant role during the initial stage, and (2) this shallow seismic swarm had slip rates consistent with those of slow earthquake processes. The proposed method will be useful in retrieving time-dependent fault slip evolution and is expected to be widely applicable to studying fault mechanics, particularly in slow earthquakes.

## Plain Language Summary

A key earthquake science challenge is to understand when an instability on a fault will arrest or run away into a large rupture. However, the slip nucleation process seems not to produce seismic waves and hence remains hidden to most seismological methods. Geodetic methods, which can directly measure motions at earth's surface, offer a complementary tool to improve our ability to map the fault slip. In this work, we expand an experimentally observed crack model, and propose a new inversion method for finding models of fault slip that can fit the observations of surface motions. The new method greatly reduces computation complexity respecting previous state-of-the-art methods, and is validated against synthetic experiments. We apply this new method to 2011 Hawthorne earthquake swarm (Nevada, USA), and discovered an aseismic slow slip before seismicity rate increased. That preparation stage was followed by a triggered larger slip on a nearby fault, and after that, the seismicity and fault slip rate reduced rapidly. We expect that this new methodology will be applied to detect similar precursory aseismic slip during long-lasting earthquake sequences, and allow us to retrieve detailed slip growth in space and time, which ultimately will advance our understanding of the faulting mechanics.



## 1 Introduction

How fault slip nucleates, grows and eventually accelerates is a critical question to describe the driving mechanisms behind earthquakes and faulting phenomena. Our current understanding is consistent but cannot distinguish among various viable mechanisms to explain how fault slip initiates: dynamic triggering (Gomberg & Johnson, 2005), tidal triggering (Delorey et al., 2017), pore-pressure diffusion (Parotidis et al., 2003) or aseismic slip (Radiguet et al., 2016; Gualandi et al., 2017; Caballero et al., 2021). In particular, Gomberg (2018) summarised two leading hypotheses for earthquake nucleation. Ranging from a stochastic model in which each earthquake triggers subsequent ones in a cascade fashion, to an alternative that favours a deterministic view where slow-slip triggers and/or precedes the occurrence of a seismically dynamic rupture. Within the scope of increasing our capacity to distinguish between the earthquake nucleation models, a promising venue is to increase our ability to image how fault slip evolves in space and time. Although fault slip evolution is not necessarily the only cause of seismicity migrating, improvements in this direction may provide crucial data to examine hypotheses for earthquake nucleation mechanisms.

Fault slip imaging improvements are particularly desirable to estimate (seismic and aseismic) slip propagation parameters, such as slip rate, and gain deeper insights into the physics controlling regular earthquakes and slow-slip phenomena. Regular earthquakes are known to show peak and average slip rates of the order of 1 m/s and 0.1 m/s (Takenaka & Fujii, 2008). While slow-slip phenomena show much lower slip rates, e.g., Slow Slip Events (SSEs), fault creep, or slip related to fluid injection. For example, in the case of SSEs in subduction zones, the peak slip rates vary around 0.1~3 cm/day (Radiguet et al., 2011; Bletery & Nocquet, 2020; Rousset et al., 2019; Ozawa et al., 2019). In the case of the episodic creep event, the slip rates in continental faults are 0.5~3 cm/year (Schmidt et al., 2005; Jolivet et al., 2012; Hussain et al., 2016; Scott et al., 2020). In fluid injection experiments, the slip rates have been observed to be much higher, up to  $4 \times 10^{-3}$  mm/s (35 cm/day) (Guglielmi et al., 2015).

Hence, to evaluate (seismic and aseismic) fault slip characteristics, a better description of how fault slip propagates in space and time is necessary. Including complex propagation patterns of fault slip such as pulse-like and crack-like ruptures (Lambert et al., 2021; Marone & Richardson, 2006). Such patterns have been observed during regular

earthquakes but are also associated with slow-slip phenomena: with slow slip transients migrating further away from where they started along strike (or dip), or remain stationary through time. Observations of some SSEs and "Episodic Tremor and Slip" (ETS) show pulse-like rupture characteristics with elongated slipping areas, e.g., the Cascadia subduction zone (Michel et al., 2019), and with along strike migration speeds of  $\sim 10$  km/day (Wech et al., 2009; Rousset et al., 2019). In contrast, slip propagation of meter-scale fluid injection experiments indicates stationary patterns: Bhattacharya and Viesca (2019) proposed a model in which the slip grows as an expanding ellipse, with the injection point as the slipping centre. The latter phenomenon is also found in some SSEs on subduction zones, e.g., the deep Manawatu and Kaimanawa SSEs on the Hikurangi subduction zone (Wallace, 2020). Here, we aim to improve fault slip mapping in space and time to contribute to the advancement of the study of fault slip processes using, yet underutilised, satellite InSAR observations.

In this research, we developed a new method to interpret directly wrapped phase InSAR observations to estimate the spatio-temporal fault slip, in particular, in the context of a favourable tectonic setting, continental seismic swarms (e.g., small-amplitude surface deformation signals and/or phase discontinuities due to surface ruptures). InSAR has been used to map surface displacements with high spatial resolution and subsequently model fault slip. But so far, it is more common to estimate static slip distributions than jointly invert for the time-series of slip evolution (Floyd et al., 2016; Ingleby et al., 2020). The problem of retrieving time series of source parameters from non-simultaneous and temporally overlapped multi-sensor observations is ill-posed; however, the oscillations of the solution caused by the rank deficiency of this problem can be reduced by applying regularisation or temporal filtering (Samsonov & D'Oreye, 2012). Grandin et al. (2010) introduced a temporal smoothing scheme as an additional constraint to retrieve the time series of magma volume changes. Additionally, González et al. (2013) used truncated singular value decomposition (TSVD) to reject model space basis vectors associated with small singular values. Instead of regularising the volume variation itself, they minimised the volume change rate, to avoid large discontinuities. Here, we improve previous methods by a) regularising the fault slip distribution using a prescribed parameterisation derived from a laboratory-based crack model, and b) introducing a statistically optimal truncation criterion that allows to automatically separate signal and noise in the spatio-temporal fault slip distributions. We demonstrated the validity of this ap-

proach using synthetic experiments and comparing it against a compilation of published slip distribution models. Finally, we applied the new proposed methodology to the 2011 Hawthorne seismic swarm (Nevada, USA). The 2011 Hawthorne seismic swarm is located at the central Walker Lane, which accommodates the Pacific-North American transform plate motion by oblique-normal faults and block rotations (Thatcher et al., 1999; Wernousky, 2005). The 2011 Hawthorne swarm consists of 10 M4+ events, and the largest earthquake among them is an M4.6 event (Zha et al., 2019; Smith et al., 2011); a recent study using satellite images reveals clear surface deformation signals before the M4.6 event, and the geodetic moment is much higher than the seismic moment, indicating that aseismic slip dominates the fault behaviour (Jiang & González, 2021). By applying our proposed methodology, we retrieved the fault-slip spatio-temporal evolution, and explored the interactions between the fault slip and the seismicity.

## 2 Time-Dependent Fault Slip Inferred Using Geodetic Fault Slip Models

### 2.1 Static Fault Slip Models

Slip inversions with kinematic models are ill-posed problems in which the solution is nonunique and unstable, and unphysical slip distributions can be estimated by least-squares algorithms, i.e., extremely rough oscillatory slip distributions. Harris and Segall (1987) introduced Laplacian smoothing as the regularisation scheme. This minimises the second derivative of slip and can prevent cases with large stress drops. Du et al. (1992) plotted a trade-off curve for misfit as a function of slip roughness, and manually picked a smoothing factor within the inflection point of the curve to find an optimal balance between data fit and model roughness. Matthews and Segall (1993) determined the optimal smoothing factor in the trade-off curve objectively by implementing the cross-validation method. Much later, Fukahata and Wright (2008) and Fukuda and Johnson (2008) introduced the Bayesian approach, ABIC (Akaike’s Bayesian Information Criterion), to solve the slip distribution. While Fukahata and Wright (2008) emphasised the significance of fault geometry as a nonlinear constraint, Fukuda and Johnson (2008) overcame the deficiencies of ABIC with positivity constraints, and then applied the adapted ABIC to simultaneously estimate the slip distribution and smoothing parameter objectively in a Bayesian framework. Fukuda and Johnson (2010) then devised a mixed linear-non-linear Bayesian inverse formulation and extended their work for the joint slip and geometry in-

version. In response, Minson et al. (2013) argued that the non-physical regularisation scheme (i.e., Laplacian smoothing) is unnecessary, and developed a fully Bayesian approach to sample all possible families of models compatible with the observations, via a parallel computing framework. Ragon et al. (2018) further extended the work of Minson et al. (2013) and accounted for the uncertainty in fault geometry. Instead of Laplacian regularisation, Amey et al. (2018) developed an inversion package *slipBERI*, and incorporated self-similarity, characterising the seismic slip distribution in real earthquakes, as a prior assumption within the Bayesian inversion of earthquake slip.

All the previous methods are based on kinematic models that do not take into account the relationship between stress and slip in the fault. Alternatively, dynamic source models satisfy physical constraints on the propagation of shear fractures on Earth, but few dynamic source models are considered to constrain the slip inversions. As an alternative, Di Carli et al. (2010) proposed using elliptical patches to describe the slip distribution in the kinematic and dynamic inversion of near-field strong motion data at low frequencies. Soon afterwards, Sun et al. (2011) put forward a *mechanical* slip inversion, imposing a uniform stress drop on the fault plane. The resulting slip distribution is inherently smooth, so the smoothing norm and the smoothing factor are unnecessary. Tridon et al. (2016) assumed a circular stress patch in volcano research, inverting the displacement for shear and normal stresses simultaneously, along with the fault geometry.

In this study, we apply a new methodology named Geodetic fault-slip Inversion using a physics-based Crack Model (GICMo) (Jiang et al., 2022). In this method, we take advantage of a one-dimensional analytical crack model proposed by Ke et al. (2020). The model was theoretically and experimentally validated in self-contained ruptures within a 3-meter-long saw-cut granite fault. This new crack model features non-singular (finite) peak stresses at the rupture tip. In Jiang et al. (2022), we expanded the one-dimensional model into two dimensions to produce elliptical fault slip shapes/patches. We assume that one of the focal points of the ellipse is the crack centre (with the maximum slip) and the elliptical perimeter to be the crack tip. Therefore, the slip distribution on the fault plane is controlled by a very compact and reduced set of parameters. The geodetic-inverted fault slip infers that it is possible that the crack centre can be located at the rupture centre, e.g., the 2009 L'Aquila earthquake (Walters et al., 2009). To adapt to this possibility, we relax the constraint that the maximum slip should coincide with the crack centre location, and allow it to move along the x axis inside the ellipse. Hence, our

crack model contains only eight parameters as demonstrated by Equation 1 and Figure 1.

$$s = \mathbf{f}(x_0, y_0, a, e, \alpha, \lambda, d_{max}, \theta) \quad (1)$$

where  $s$  is the slip distribution;  $x_0, y_0$  are the locations of the crack centre ;  $a$  and  $e$  are the semi-major axis and eccentricity of the ellipse;  $\alpha$  is the ratio controlling the location of the crack centre along x axis: the crack centre is located at the ellipse centre , left/right vertices when  $\alpha = 0, -1/1$ ;  $\lambda$  is the ratio controlling the displacement transition from the centre to the edge of the elliptical crack;  $d_{max}$  is the maximum slip;  $\theta$  is the rake angle.

In the GICMo method, once the crack model parameters are provided, the slips for all fault patches are then determined based on the two-dimensional crack model discussed above. Then, the fault slip distribution is forward modelled to estimate surface displacement. Following Jiang and González (2020), a misfit function is constructed based on the wrapped phase residuals and the weighting matrix. The misfit function is then regarded as the likelihood function fed into the Bayesian process to retrieve the posterior distribution of crack model parameters. In the Bayesian process, the Markov chain Monte Carlo algorithm is adopted as the probability sampling approach based on the Metropolis-Hasting rule.

Here we design a synthetic static slip to compare the performance of our method, GICMo, and a state-of-the-art method, slipBERI (Amey et al., 2018). The geodetic inversion package, slipBERI, solves for fault slip with GNSS and unwrapped InSAR phases in a Bayesian approach using von Karman regularisation, and simultaneously solves for a hyperparameter that controls the degree of regularisation. A normal fault with pure down-dip slip is simulated as the synthetic fault model. To imitate the slipping patterns observed in the published finite-source rupture models SRCMOD (Mai & Thingbaijam, 2014) (e.g., Bennett et al. (1995), Ichinose et al. (2003), and Elliott et al. (2010)), the inner region is a square area with a larger displacement, and the outer region is an annulus area with a smaller displacement (Figure 2). Due to the difference in the ingestion data, the synthetic phases are unwrapped phases for slipBERI and wrapped phases for GICMo. The displacement phase is forward calculated based on the synthetic fault slip distribution and the dislocation model. To increase its resemblance to reality, decorrelation and atmosphere noises are simulated and added, whose amplitudes are 10% of  $2\pi$  for wrapped phase cases or the peak amplitude of the deformation phase for unwrapped

phase cases, which is based on the signal-to-noise ratio from a real interferogram in Section 4 (RS2-20110322-20110415). The simulated noise-plus-deformation interferogram is resampled with a quadtree algorithm within the downsampled unwrapped and wrapped phases (Bagnardi & Hooper, 2018; Jiang & González, 2020). In addition, the covariance matrix is estimated based on the phase in the far-field. Finally, the downsampled phases and covariance matrix are fed into slipBERI and GICMo to retrieve the slip distributions. Figures 2b-2d show the modelled slip distribution inverted by GICMo and slipBERI, and Figure S1 shows the modelled phase and phase residuals. The conclusions are listed below.

- (1) Both GICMo and slipBERI provide the first-order accuracy of the slip distribution, including the locations of the crack centre and the magnitude of the slip peak.
- (2) We interpolate the slip distribution onto a  $0.5 \text{ km} \times 0.5 \text{ km}$  patch mesh, and calculate the root-mean-square error (RMSE) of the slip distribution compared with the synthetic slip distribution. We find that the RMSEs are 1.5 cm for the one-ellipse model, 2 cm for the von Karman smoothing model, and 3 cm for the Laplacian smoothing model, which are approximately similar. However, the great advantage is that the parameters to be solved in GICMo are independent of the fault mesh discretization, and the number of parameters is 30 times less in this case than 201 in slipBERI for this case.

## 2.2 Bayesian Inversion of Fault Slip Time-Series Using a Physics-based Crack Model (Time-GICMo)

The temporal evolution of fault slip is critical to understanding the driving mechanism of slow slip. It is difficult to find one slow slip event where one interferogram can coincidentally capture the beginning and the ending of the activity. Instead, a common scenario is that the slip increment is captured by interferograms. In this section, we develop a new method of retrieving the slip increments and demonstrate the time-series slip estimation with synthetic experiments. Assuming two elliptical ruptures at the beginning and the ending, slip increment  $\Delta s = s^2 - s^1$ , where  $s^2$  and  $s^1$  are the slip distributions at the end and the beginning of the interferogram.

We consider a system of  $N$  increments of fault slip ( $\Delta s^n \in [\Delta s^1, \dots, \Delta s^N]$ ) between dates  $t_i^n$  and  $t_j^n$ ) based on the non-linear inversion estimation from the corresponding wrapped interferogram, and the raw images of interferograms are acquired at  $M$  unique dates ( $t \in [t_1, \dots, t_M]$ ). The aim is to solve for the temporal evolution of fault slips ( $s \in [s_1, \dots, s_M]$ )

for each date. We assume that the slip rate between adjacent dates ( $v_m \in [v_1, \dots, v_{M-1}]$ ) is constant, so the slip increment  $\Delta s^n$  can be expressed by the sum of fault slip increment between adjacent dates,  $\Delta s^n = \sum_{m=i}^{j-1} v_m (t_{m+1}^n - t_m^n)$ . The linear expression for  $N$  increments of fault slip is shown in Equation 2, as illustrated by González et al. (2013):

$$\begin{aligned} \mathbf{P} &= \mathbf{B}\mathbf{Q} \\ \mathbf{P} &= [\Delta s^1 \quad \dots \quad \Delta s^n \quad \dots \quad \Delta s^N]^T \\ \mathbf{Q} &= [v_1 \quad \dots \quad v_m \quad \dots \quad v_{M-1}]^T \\ \mathbf{B}(n, m) &= \begin{cases} t_{m+1}^n - t_m^n, & \text{if } i \leq m \leq j - 1. \\ 0, & \text{otherwise.} \end{cases} \end{aligned} \quad (2)$$

where  $\mathbf{P}$  is the observation vector,  $\mathbf{Q}$  is the unknown vector, and  $\mathbf{B}$  is the designed matrix. Considering there are  $N$  increments of fault slip, the matrix dimension is  $(N \times 1)$  for  $\mathbf{P}$ ,  $(N \times (M - 1))$  for  $\mathbf{B}$ , and  $((M - 1) \times 1)$  for  $\mathbf{Q}$ . Then, we decompose matrix  $\mathbf{B}$  by using the SVD methods,

$$\mathbf{B} = \mathbf{U}\mathbf{S}\mathbf{V}^T \quad (3)$$

where  $\mathbf{U}$  is an orthogonal matrix with columns that are the basis vectors of the data space ( $N \times N$ ),  $\mathbf{V}$  is an orthogonal matrix with columns that are the basis vectors spanning the singular values of the model  $((M - 1) \times (M - 1))$ , and  $\mathbf{S}$  is a diagonal matrix of the singular values  $((N \times (M - 1)) \times 1)$ . A solution for this problem can be obtained as follows,

$$\mathbf{Q} = \mathbf{V}\mathbf{S}^{-1}\mathbf{U}^T\mathbf{P} \quad (4)$$

If  $\text{rank}(\mathbf{B}) < m$ , the solution obtained using the SVD technique may contain numerical instabilities when there are small singular values. In this case, a more stable solution can be achieved using the TSVD method (Aster et al., 2019), which rejects model space basis vectors associated with small singular values, up to a certain threshold. As an improvement upon González et al. (2013), we apply an optimal hard threshold for singular values truncation proposed by Gavish and Donoho (2014). Gavish and Donoho (2014) proposed that the optimal hard threshold for singular value is  $4/\sqrt{3}$  of the median singular value. This criterion is empirically proven to be the best hard thresholding, independent of model size, noise level, or true rank of the low-rank model. This improvement

allows us to define the degree of regularisation based on an objective criterion, which generates a parsimonious low-rank model solution in the presence of noisy data. Note that in order to retrieve a realistic solution, a non-negative constraint is added in solving for slip rate vector  $Q$  implemented by using MATLAB function *lsqnonneg* (<https://uk.mathworks.com/help/optim/ug/lsqnonneg.html>). It is physically appropriate because slip along faults rarely re-rupture backwards (Hicks et al., 2020).

### 3 Time-dependent Fault Slip Inversion Experiments

In this section, we describe two experiments to investigate if this method can retrieve pulse- and crack-like rupture propagation patterns in space and time. We tested the performance of the inversion method to recover fault slip evolution from each of the two-ellipse models.

The first synthetic case aims to explore the inversion with overlapping ruptures (Figure 3). Several recent studies have suggested spatial overlap between coseismic slip and afterslip (Barnhart et al., 2016; Bedford et al., 2013; Bürgmann et al., 2002; Johnson et al., 2012; Pritchard & Simons, 2006; Salman et al., 2017; Tsang et al., 2016). A series of overlapping elliptical cracks are simulated in Figure 3a, and a forward inversion is performed to calculate the surface displacement due to the slip increment between adjacent cracks. We aimed to compare the results based on various geodetic inversion algorithms: (1) the one-ellipse model, as described in Section 2.1, (2) a von Karman regularisation algorithm (Amey et al., 2018), (3) the two-ellipse model with different crack centres. Inversion results are shown in Figures 3b-3d, and the modelled phase and residuals are shown in Figures S2-S3. The main conclusions are as follows.

(1) The RMSEs of the fault slip residual is the lowest in results based on the two-ellipse model with different centres. The triangle patch size in the crack model is  $\sim 0.84$  km, and the rectangle patch size in slipBERI is 1.5 km. In this way, we interpolated the modelled slip distributions to grid points with 1.17 km spacing, and then calculated the RMSE of the fault slip residual. In each case, the RMSE of slip residuals based on the two-ellipse model with different centres (Figure 3d) are the smallest, and the average RMSE for the one-ellipse model, the von Karman smoothing model and the two-ellipse model are 0.9 cm, 1.6 cm, and 0.6 cm.

(2) The two-ellipse model is superior to the one-ellipse model in the F-test for the residual of the interferometric phase. The two-ellipse model has more free parameters,



leading to an inherent improvement in the data fit. To objectively compare the model performances, we use the F-ratio statistic to test the significance of the decrease of residuals between models (Stein & Gordon, 1984). The statistical test checks if the empirical F-ratio ( $F_{emp}$ ) is larger than the theoretical ( $F_{theory}$ ). In this case, the comparison of the one-ellipse model and two-ellipse model leads to  $F_{emp} = 72.8 \gg F_{theory} = 2.6$ .

The second synthetic case aims to explore the inversion with the containing ruptures (Figure 4). A growing rupture has been widely observed and studied in fluid injection experiments (Guglielmi et al., 2015; Bhattacharya & Viesca, 2019; Cappa et al., 2019). The rupture centre is located at the injection point, and the radius of the slipping zone grows at a rate up to  $10^{-6}$  m/s. A set containing elliptical ruptures is simulated in Figure 4a, and a forward inversion facilitates the surface displacement calculation. We aimed to retrieve the slip increments from the observed interferometric phase with various methods described above (one-ellipse model, von Karman smoothing model, and two-ellipse model). On noticing that the slip distribution is not well resolved by the two-ellipse model with different centre  $s$ , we added another constraint to the two-ellipse model so that both cracks share the same centre. The inversion results are shown in Figures 4b-4e, and the modelled phase and residuals are shown in Figures S4-S5. The main conclusions are as follows.

(1) The average RMSE of slip residuals based on various inversion models (one-ellipse model, von Karman smoothing model, two-ellipse model with different centre  $s$ , and one centre) are 1.3 cm, 1.3 cm, 1.0 cm, and 0.8 cm. The one-ellipse model failed because the slip increment in containing ruptures no longer could be described by one complete crack. Indeed, slipBERI showed better performance because it inferred the region with the slip peak. The two-ellipse model with different centres is even better but was not well resolved, e.g., the slip increment from  $t_1$  to  $t_2$  (second image in Figure 4c). Therefore, the two-ellipse model with the *same* centre is the most appropriate for reconstructing the cracks' locations, sizes, and maximum slips.

(2) In the F-test of the interferometric phase residuals, the two-ellipse model with the same centre is superior to the two-ellipse model with different centre  $s$ , and the one-ellipse model is the least useful.

## 4 Application case: the 2011 Hawthorne Seismic Swarm (Nevada, USA)

### 4.1 Regional Tectonics and Seismicity

We apply our algorithm to the 2011 Hawthorne seismic swarm, which occurred on the central Walker Lane (Figure 5). The Walker Lane is a 500 km-long and 100 km-wide deformation region consisting of N-NW right-lateral shear and extension (Wesnousky, 2005). It is located between the northwest translating Sierra Nevada microplate and the westward extending Basin and Range Province. The Walker Lane accommodates 20%  $\sim$  25% of the current relative motion (50 mm/year) between the Pacific and North American plates (Argus & Gordon, 1991; Faults & Henry, 2008). The central Walker Lane accommodates the deformation budget of  $\sim$ 8 mm/year between the Basin and Range province and the central Sierra Nevada (Bormann et al., 2016). The distributed dextral shear in central Walker Lane is accommodated by oblique-normal faults, block rotations, and partitioning of oblique deformation between sub-parallel normal and strike-slip faults. The total long-term strain rate is 51 nanostrain/year extension directed N77°W and 38 nanostrain/year contraction directed N13°E (Kreemer et al., 2014), much higher than the central Basin and Range (Kreemer et al., 2009).

Being a geologically young and developing fault system, the Walker Lane shows high levels of seismicity over the instrument period, including  $>10$  M6+ earthquakes in the last century. Since 2000, the Walker Lane was struck by a few seismic sequences with some accompanied by aseismic slip evidence. For example, for the 2008 Mogul earthquake sequence, geodetic observation and modelling indicated significant aseismic slip (Bell et al., 2012), and the migration speed of the largest foreshock cluster is consistent with aseismic slip (Ruhl et al., 2016); for the 2014 Virginia City Swarm, migration rate of small earthquakes was consistent with rates observed elsewhere associated with pore fluid diffusion and aseismic creep (Hatch et al., 2020). However, there was no clear indication of aseismic slip during the 2016 Nine Mile Ranch sequence (Hatch-Ibarra et al., 2022), the 2017 Truckee sequence (Hatch et al., 2018) or the 2020 Monte Cristo Range sequence (Ruhl et al., 2021).

The 2011 Hawthorne seismic swarm lasted from March to September and consisted of 10 M4+ earthquakes according to the U.S. Geological Survey (USGS) hypocentre catalogue (<https://earthquake.usgs.gov/earthquakes/search/>). This sequence occurred in the footwall block of the Wassuk Range segment at the central Walker Lane (Faults

& Henry, 2008), and this segment experiences a significant extension of  $1.5 \pm 0.3$  mm/year (Hammond & Thatcher, 2007). Early moment tensor solutions show the shallow depths in this sequence (Smith et al., 2011), and further hypocentre relocation together with the focal mechanisms of the M4+ events consistently reveal a W-NW-dipping normal fault zone with centroid depths between 2 km and 4 km (Zha et al., 2019). The 2011 Hawthorne sequence is close to the Aurora-Bodie volcano (Lange & Carmichael, 1996), but no volcanic signature was observed in near-source seismograms, which infers this sequence is not likely related to the magmatic activity (Smith et al., 2011; Zha et al., 2019). In this research, we were able to identify three stages with respect to the timing of the most energetic event (M4.6) occurred: an initial stage (pre-M4.6 stage) from 15 March to 17 April, a shorter period around the most energetic stage (co-M4.6 stage), and the post-energetic stage (post-M4.6 stage) lasting until 17 September.

## 4.2 Multi-satellite Geodetic Datasets

We processed ENVISAT and RADARSAT-2 data and generated 8 SAR interferograms to quantify surface displacements (Figure 6). SAR images were acquired between February and September 2011 from two tracks: one ascending track from the Canadian Space Agency RADARSAT-2 satellite, look angle of  $35^\circ$  and heading angle of  $350^\circ$ ; and another descending track from the European Space Agency (ESA) ENVISAT satellite, track 343, look angle of  $35^\circ$  and heading angle of  $-166^\circ$ . Interferograms were processed in two-pass differential mode, using a 30 m resolution digital elevation model (DEM) derived from the Shuttle Radar Topography Mission. ENVISAT-ASAR data were processed using Doris software (Kampes et al., 2003) and ISCE software, RADARSAT-2 data using GAMMA software (Werner, 2000). Overall, we obtained 8 short baseline differential interferograms. The computed interferograms have temporal separations ranging from 24 to 120 days. Considering the dominant extensional mechanism and N-S fault striking in this region, the preferred movement direction of the ground displacement is E-W. Consequently, the satellite flight direction favours surface displacement observations in this normal faulting system.

Interestingly, 2 ascending RADARSAT-2 interferograms during the pre-M4.6 stage indicated clear surface displacement signals (Figure 6d and 6a),  $\sim 4$  cm away from satellite line-of-sight motion. In interferograms covering the co-M4.6 stage, it is notable that surface displacement signals were larger in magnitude and located further north with re-

spect to the pre-M4.6 stage (Figures 6b, 6c, 6e and 6f). During the early post-M4.6 stage, surface displacements were detected along a very narrow spatial band with clear phase discontinuities, suggesting surface ruptures (Figure 6g). For one interferogram covering the late post-M4.6 stage (Figure 6h), the phase was dominated by atmospheric noise and no clear deformation signal was detected. Analysis of interferograms suggests that fault slip may have occurred along a fault system with a two-plane geometry, which is consistent with the finding from early moment tensor solutions (Smith et al., 2011).

Note that the 2 ascending RADARSAT-2 interferograms provide a unique opportunity to look into the preseismic slip, which is not available in other reported cases due to the data limitation. For example, for the 2008 Mogul earthquake swarm, Bell et al. (2012) measured the surface deformation covering the whole earthquake swarm using InSAR and they found that the modelled cumulative geodetic moment is  $\sim 2$  times the cumulative seismic moment, indicating a significant portion of aseismic slip. However, they cannot separate the preseismic deformation signal because there is no available interferogram covering the preseismic stage only. In addition, the GPS observations covering the 2008 Mogul earthquake swarm cannot constrain the preseismic slip well due to the low signal to noise ratio in GPS solutions (Ruhl et al., 2016).

### 4.3 Spatio-temporal Slip Evolution

To develop the kinematic fault model, we first constructed the fault geometry derived from a non-linear fault inversion of InSAR wrapped phase observations, solving for uniform distribution on rectangular faults (Jiang & González, 2020). A geodetic inversion directly using the interferometric wrapped phase avoids any potential phase unwrapping error (Figure S6). The data variance-covariances describing the noise level are calculated based on the covariograms (Figure S7) and are used to weight the wrapped phase residuals in the likelihood function as illustrated by Jiang and González (2020). Modelling of a selection of interferograms covering the successive phases confirmed that ground motion could be caused by fault geometry with two distinct planes. During the pre-M4.6 stage, the observed ground motion in the RADARSAT-2 interferogram (2011/03/22-2011/04/15, Figure 6d, and fault-normal profile in Figure 7d) would be consistent with slip along a N-S striking normal fault to the south (green rectangular fault in Figure 7a). After modelling the interferogram covering the co- and post-M4.6 stages (2011/04/15-2011/06/26, Figure 6f, and fault-normal profile in Figure 7c), Figure 6f shows a different fault seg-

ment on a NE-SW trending normal fault to the north (yellow rectangular fault in Figure 7a). Only one single fault is applied in the modelling above, and the phase caused by the northern subfault is modelled well due to its dominance during the co- and post-M4.6 stages. The residual is relatively larger in the south because of the ignorance of the southern subfault, as shown by the residual phases in Figure S8. Based on modelled fault geometry in Figure 7a, together with ground motion discontinuities digitised from the interferograms, we constructed a smooth fault plane with uniformly discretized triangular meshes in Figure 7d. These were generated by FaultResampler (Barnhart & Lohman, 2010) and mesh2d (Engwirda, 2014), with a near-uniform side length of around 125 m. Then, a fault slip distribution model with associated uncertainties was estimated. We applied the fault slip inversion method based on a prescribed regularisation derived from an experimentally validated physics-based crack model (Jiang et al., 2022). To further investigate the temporal evolution of fault slips with a higher temporal resolution, we invert the fault slip time series using all available interferograms with clear deformation signals.

Figure 8 presents the temporal evolution of cumulative slip and slip rate during the 2011 Hawthorne seismic swarm, and Figure S9 shows the modelled phase and phase residuals. The findings from the inversion results are listed as follows.

(1) There were three areas with different spatio-temporal slipping behaviours: a narrow ( $5 \text{ km}^2$ ) slip area on the southern fault with a high rate (with a lower bound:  $1.5 \text{ cm/day}$ , or  $1.7 \times 10^{-7} \text{ m/s}$ ) occurring during the pre-M4.6 stage, a wider ( $15 \text{ km}^2$ ) slip area with lower average slip ( $10 \text{ cm}$ ) on the northern fault that ruptured during the co-M4.6 stage, and a shallow slip area (depth= $1 \text{ km}$ ) just above the second area during the post-M4.6 stage with a slower average slip rate (with a lower bound:  $0.2 \text{ cm/day}$ , or  $2.3 \times 10^{-8} \text{ m/s}$ ).

(2) Our results show the aseismic slip mainly occurred on the southern subfault during the pre-M4.6 stage, while the most significant seismic slip hit the northern subfault during the co- and post-M4.6 stages. The results are more consistent with a cascade model of discrete slip patches, rather than a slow-slip model considered as a growing elliptical crack.

(3) During the early pre-M4.6 stage (February 26-March 22), the cumulative geodetic moment is  $1.7 \times 10^{16} \text{ Nm}$  (equivalent to an  $M_w$  4.7 event), 45 times as large as the cumulative seismic moment ( $0.04 \times 10^{16} \text{ Nm}$ ). The cumulative geodetic/seismic moment ratio reduces over time, but remains larger than 3 during the co- and post-M4.6 stages.

## 5 Discussion

### 5.1 On the Spatial Complexity of Fault Slip Distributions

Fault slip most likely has non-uniform spatial distribution due to spatial heterogeneities of rock strength and stress state on the fault, with well-known dependence on depth and the less understood along-strike variations. Seismic and geodetic inversions can reveal how fault slip is distributed on the discretized fault plane. However, to explore all possible models consistent with observations, the parameter space scales up rapidly to a large number of unknowns, increasing the problem's null-space, which means there are many vectors in the model space that are unconstrained by the data. Therefore, it is reasonable to consider our understanding of the complexity of slip distribution in natural earthquakes. The reasonable approach can allow for fault-slip heterogeneity while keeping the problem null-space as small as possible. Mai and Beroza (2002) compiled published finite-source rupture models and proposed the fractal pattern in slip distributions. It is true for large earthquakes, and multiple fault segments with several rupturing centres are revealed by geodetic and seismological observations, e.g., the 2008  $M_w 7.9$  Wenchuan earthquake (Shen et al., 2009), and the 2016  $M_w 7.8$  Kaikoura earthquake (Hamling et al., 2017). However, solving a huge number of parameters has a high computation cost. Computation complexities in their algorithms depend greatly on the number of discretized fault patches. For example, when studying a 40 km-long and 20 km-wide fault with slip-*BERI*, there are 200 patches if the patch size is 2 km and the parameter's dimension is 400. The latter would rapidly increase to 1600 if the patch size is 1 km. This is possibly the reason why the number of imported fault patches has upper bounds in practice, particularly if a Bayesian sampling strategy is employed. Though techniques like parallel computing have been introduced to improve computation efficiency, sampling such high-dimensional problems is still computationally challenging and does not solve the size of the null-space.

In this research effort, we favoured a method that dramatically reduces the number of free parameters to solve; the drawback is that it results in *compact* fault slip distributions. However, our inverted slip distribution patterns are supported by the observations. This is a reasonable approach because many inversion results support fault-slip distributions that are spatially compact, especially for small-magnitude earthquakes (Taymaz et al., 2007; Barnhart et al., 2014; Xu et al., 2016; Champenois et al., 2017; Ainscoe et

al., 2017). Many studies have successfully modelled the majority of surface displacement signals using only one single fault with uniform distribution (Biggs et al., 2006; Nissen et al., 2007; Walters et al., 2009). For slow slip events across the global subduction zones, distribution patterns usually follow an elliptical shape with one slipping centre (Wallace et al., 2012; Villegas-Lanza et al., 2016; Fukuda, 2018), and the fractal pattern is not required.

Benefiting from the online database of finite fault rupture models, SRCMOD (Mai & Thingbaijam, 2014), we were able to quantitatively evaluate how well a single elliptical model fits the available slip distributions across various tectonic settings and magnitudes. We retrieved 300 slip distributions on a single fault from SRCMOD and intended to model the slip distributions with the one-ellipse model. Our experiments showed that for 85% of  $M_w \leq 7.5$  events, the RMSE of the slip residual is less than 20% of the peak slip (Figure S10). In addition, a simple circular crack is also the widely accepted assumed model in stress drop estimation based on seismic spectra (Madariaga, 1976; Kaneko & Shearer, 2014). Though only small degrees of freedom are allowed in the one-ellipse model, complexity could be added by incorporating multiple ruptures. As we showed in Section 2.2, a half-moon pattern was retrieved by two containing or overlapping elliptical crack models. Similarly, it is possible to overlap multiple ruptures to simulate multiple peak slips or more complex patterns.

The compact slip distribution in this new elliptical model is also favourable to evaluate the statistics of small earthquakes. Earthquake source parameters characterisation of small earthquakes is important for understanding the physics of source processes and might be useful for earthquake forecasting (Uchide et al., 2014). A wide-used source model to analyse the source parameters of small earthquakes is a circular crack rupture (Brune, 1970; Madariaga, 1976) with stress singularity at the crack tip, and we hope our new elliptical slip model, which avoids this stress singularity, can be an alternative source model in the future (Shearer et al., 2006). Furthermore, by taking advantage of the improved method for estimating slip rates during temporally overlapping InSAR timeframes, one can image the fault behaviour over a long period in a relatively high temporal resolution. This new method is expected to be applied to investigate the temporal evolution of slow fault slip, e.g., transient slow slip (Khoshmanesh et al., 2015; Kyriakopoulos et al., 2013; Klein et al., 2018), afterslip (Thomas et al., 2014), and slow slip events in subduction zones (Bletery & Nocquet, 2020; Rousset et al., 2019; Ozawa et al., 2019).

## 5.2 Time-dependent Fault Kinematics during Continental Seismic Swarms and Other Slow Earthquakes

During the initial stage of the 2011 Hawthorne seismic swarm, a substantial amount of aseismic slip ruptured on the southern subfault without strong seismicity (e.g., the first two periods in Figure 8b), with peak slip rates of 1.1~5.4 cm/day, average slip rate 0.4~1.9 cm/day and migration velocity 0.05 km/day. Note that these values are lower bounds, as the time between two neighbouring epochs ( $\Delta s^n$ ) of SAR image acquisition time may be longer than the duration of slow slip events, preventing capture of short events with higher velocities. The limitation due to the temporal sampling of InSAR could be improved by combining all of the InSAR datasets, or incorporating other high-temporal resolution observations, e.g., GNSS or strainmeter observations. We anticipate that the current InSAR temporal sampling limitation will be reduced over the second half of this decade (2020s). Our approach will be well suited to fully utilise the multiconstellation of InSAR capable satellites (Sentinel-1, CosmoSky-Med, PAZ, TerraSAR-X, ALOS-2, ALOS-4, NISAR, etc.). The phenomena potentially driven by aseismic slip are widely explored, e.g., ETS, Rapid Tremor Reversals (RTRs), SSEs, fault creep, and fluid injection. To better compare this precursory aseismic slip with other identified phenomena in the slow slip family, we compile the slip rates and migration velocities found in the literature (list below and in Table S1).

(1) The peak slip rate. SSEs show a wide range of peak slip rates among subduction zones, e.g., 0.27 cm/day for the Cascadia subduction zone (Bletery & Nocquet, 2020), 0.3 cm/day for South Central Alaska Megathrust (Rousset et al., 2019), 0.6~2.8 cm/day for Japan trench (Hirose & Obara, 2010; Ozawa et al., 2019). During the early stage of the 2011 Peloponnese seismic swarm (Greece) (Kyriakopoulos et al., 2013), the fault behaviour was dominated by aseismic slip inferred from the geodetic and seismic moment, and the peak slip rate was 0.26 cm/day. The maximum slip rate in fault creep events is very low, e.g., 0.5 cm/year on the Hayward fault (Schmidt et al., 2005), 0.5 cm/year on the Haiyuan Fault (Jolivet et al., 2012; Song et al., 2019), 0.8 cm/year on the North Anatolia Fault (Hussain et al., 2016) and 3 cm/year on the San Andreas Fault (Johanson & Bürgmann, 2005; Khoshmanesh et al., 2015; Scott et al., 2020). However, in the fluid injection experiment the slow aseismic slip during the early stage was much higher,  $4 \times 10^{-3}$  mm/s (35 cm/day) (Guglielmi et al., 2015), potentially because the measurement



in the fluid injection is real-time, and the duration uncertainty is much lower than SSEs observations.

(2) The average rate of slip increment. Research on the 2010-2014 seismic swarm in southern Italy (Cheloni et al., 2017) is consistent with our findings. This research revealed that the average slip rate started to increase two months before the largest shock ( $M_w 5.1$ ) and reached the highest value,  $\sim 0.1$  cm/day, a few days before the largest shock. It then decreased to zero in the following months. This highest average slip rate was at the same level with  $\sim 0.4$ - $1.9$  cm/day in our research. The aseismic slip rate inferred by SSEs is lower,  $\sim 0.03$ - $0.14$  cm/day (Radiguet et al., 2011), and this value is much lower inferred by RE,  $\sim 0.3$ - $3$  cm/year (Nadeau & McEvilly, 1999; Turner et al., 2013; Mesmeri & Karakostas, 2018).

(3) Migration velocity. These velocities of ETS and SSEs vary with subduction zones (Yamashita et al., 2015), but the generally reported migration velocity along the strike of the plate geometry is  $\sim 10$  km/day (Wech et al., 2009), while RTRs propagate ‘backwards’ 20 to 40 times faster than ETS advances (Houston et al., 2011). The large-scale features of ETS propagation with RTRs are reproduced and supported by numerical experiments (Luo & Liu, 2019; Liu et al., 2020). Similarly, migration velocity in TES varies over a wide range, from 0.5 to 14 km/day (Passarelli et al., 2018; De Barros et al., 2020).

### 5.3 Spatially variable mechanical response of the Hawthorne swarm faults

As shown in Figure 8b, the southern segment is active during the pre-M4.6 stage, and the fault behaviour is mostly dominated by aseismic slip, inferred from a very high geodetic/seismic moment ratio, 45 (Figure 8c), while the general cumulative geodetic/seismic moment ratio remains larger than three for the whole seismic swarm. This significant portion of aseismic slip identified here has been reported to explain the discrepancy between the geodetic moment and the seismic moment in a handful of continental seismic swarms (Lohman & McGuire, 2007; Wicks et al., 2011; Kyriakopoulos et al., 2013; Guandalini et al., 2017; Cheloni et al., 2017). In 2005, a tectonic swarm of over a thousand earthquakes occurred in the Salton Trough, California (USA) and Lohman and McGuire (2007) revealed the geodetic moment of the modelled fault system was about seven times the cumulative seismic moment of the swarm. Wicks et al. (2011) studied a swarm in southeastern Washington (USA) and also found the geodetic/seismic moment ratio was about

seven. During the 2011 Peloponnese Peninsula seismic swarm (Greece), Kyriakopoulos et al. (2013) revealed a big discrepancy in moment release, where the geodetic moment was  $\sim 5$  times the cumulative seismic moment for the interval July 3-October 1. For the 2013-2014 Northern Apennines seismic swarm (Italy), the moment associated with aseismic deformation/the seismic moment ratio is between  $70\% \pm 29\%$  and  $200\% \pm 70\%$  (Gualandi et al., 2017). For the 2010-2014 Pollino seismic swarm (Italy), Cheloni et al. (2017) found that 70% of the moment was released aseismically. Above all, previous studies require aseismic slip to explain the discrepancy between the geodetic moment and seismic moment for seismic swarms, with the estimated ratio of  $\sim 1.7-7$ . Furthermore, the compact fault slip identified during the pre-M4.6 stage is favoured by our improved methodology as demonstrated in Section 2. The previous finding of fractal distribution of fault slip is based on M5.9+ earthquakes (Mai & Beroza, 2002), while small-to-moderate-magnitude ruptures would have a more compact slip distribution with low complexity as observed in the rupture models SRCMOD (Mai & Thingbaijam, 2014). Therefore, we hope that our improved method can be used to improve the detection of similar small-to-moderate-magnitude aseismic transients in future seismic swarms.

The large disagreement between the geodetic moment and the seismic moment indicates that aseismic slip dominates the fault behaviour during the early stage of the 2011 Hawthorne seismic swarm, and seismic slip cannot solely explain the observed surface deformation successfully. Thus, the nucleation of the M4.6 event does not follow the cascading model, which only depends on the stress transfer caused by neighbouring foreshocks and aseismic slip is not involved. Here we test whether the nucleation of the M4.6 event follows another earthquake nucleation hypothesis, the preslip model, where the stress transfer caused by aseismic slip is responsible for the largest shock's occurrence. We utilise the cumulative slip distribution from our inversion model and compute the Coulomb stress change on the fault geometry as shown in Figure 8. The cumulative fault slip caused a Coulomb stress increase over the seismic rupture region of the M4.6 event and the maximum value is  $4.1 \text{ MPa} > 0.01 \text{ MPa}$ , which is enough to trigger an earthquake (King et al., 1994). In addition, we compute the Coulomb stress change caused by a seismic slip of foreshocks on the fault geometry, and we find that the maximum Coulomb stress increase over the seismic rupture region of the M4.6 event is  $1.5 \text{ MPa} > 0.01 \text{ MPa}$ , so the cascading model may also play a role in the nucleation process. Note that the stress change analysis based on foreshocks' locations can be affected by many factors, e.g., the preci-

sion of earthquake hypocentre, and the stress drop calculation method. For example, an  $M_w$  4.3 foreshock occurred two hours before the 1992  $M_w$  6.1 Joshua Tree earthquake, and there are opposite conclusions on whether the mainshock is triggered by the foreshock, by using different spatial resolutions in the foreshock-location-based analysis performed by Dodge et al. (1996) and Mori (1996). Therefore, because the Coulomb stress increase cause by aseismic slip is larger than that caused by seismic slip,  $4.1 \text{ MPa} > 1.5 \text{ MPa}$ , we interpret that the largest M4.6 event could have been triggered by earthquake nucleation initiated by aseismic slip, but the nearby preceding foreshocks likely also contributed to the nucleation process.

The aseismic slip mainly occurred on the southern subfault during the pre-M4.6 stage, while the most significant seismic slip hit the northern subfault during the co- and post-M4.6 stages. Here we discuss the possible underlying mechanisms of contrasting behaviours on the two subfaults. One potential cause of the precursory aseismic slip on the southern segment is various dilatancy properties along the strike. Many authors have studied the shear-induced dilatancy, which could increase the effective normal stress and thus favour fault stability (Segall & Rice, 1995; Segall et al., 2010; Ciardo & Lecampion, 2019). For example, to explain abundant microseismicity and aseismic transients in barrier zones on the Gofar transform fault, Liu et al. (2020) proposed a numerical model where strong dilatancy strengthening effectively stabilizes along-strike seismic rupture propagation and results in rupture barriers where aseismic transients arise. If this is also true for the 2011 Hawthorne seismic swarm, the shear-induced dilatancy would explain the aseismic transients on the southern fault and the seismic rupture on the northern subfault. What's more, the requirement of enhanced fluid-filled porosity for the dilatancy strengthening might be filled for the 2011 Hawthorne sequence. The 2011 Hawthorne sequence is close to the Aurora-Bodie volcano (Lange & Carmichael, 1996), and geothermal fluids have been found in this area (Hinz et al., 2010), so it is possible that excess fluids can be persistently supplied and lead to large fluid-filled porosity and high pore pressure. Therefore, the dilatancy strengthening might be one of the underlying mechanisms that govern the partitioning between aseismic and seismic slip during the 2011 Hawthorne earthquake swarm.

In addition, the fault geometrical complexity could favour the lateral variation of slip and aseismic slip. Firstly, Romanet et al. (2018) proposed that two overlapping faults can naturally result in a complex seismic cycle without introducing complex frictional

heterogeneities on the fault. They found that for two mildly rate-weakening faults with a small distance between the faults, a complex behaviour with a mixture of slow and rapid slip can be observed. This finding is consistent with the mixture of slow and fast slip close to the connecting region of two subfaults during the 2011 Hawthorne swarm (triangular subfault in Figure 8). Secondly, Cattania and Segall (2021) highlights the effect of long-wavelength fault roughness on a range of fault behaviours, foreshocks, and precursory slow slip, during the preparation stage of an energetic event. Their numerical simulation suggested the preparation stage is characterised by feedback between creep and foreshocks: episodic seismic ruptures break neighbouring asperity groups and favour the creep acceleration, which loads other asperities leading to further foreshocks consecutively. The coexistence of foreshocks and precursory slow slip, as well as their migration toward the hypocentre of the energetic event in Cattania and Segall (2021), also matched our observation during the pre-4.6 stage (Figure 8). Therefore, we think fault geometrical complexity might contribute to the precursory slow slip during the 2011 Hawthorne earthquake swarm.

## 6 Conclusion

This study developed a new methodology for estimating time-dependent fault slip distributions, by incorporating a physics-based crack model as a regularisation term. We first introduce two propagation patterns of fault ruptures and then propose a method to solve the complex slip distribution with multiple physics-based crack models. Finally, the performance of the proposed methodology is analysed with simulated experiments and geodetic observations during a real seismic swarm case. The advantages of the proposed method are as follows.

(1) The estimated fault slip solutions describe a compact slip distribution, due to the use of a laboratory-derived crack model. This choice significantly reduces the number of parameters to solve, independently of the subsequent level of fault discretization. Though the slip complexity is less than in the previous methods, the additional complexity in the slip pattern can be incorporated by incorporating multiple partially or totally overlapping elliptical cracks.

(2) The robustness of our method has been analysed by a) its capability to reproduce synthetic simulated cases with various slip patterns, and by b) the ability of elliptical slip patterns to reproduce published slip distribution from the SRCMOD database.

(3) Our proposed method is applied to estimate a detailed time-dependent fault slip distribution model for the 2011 Hawthorne seismic swarm (Nevada, USA). Our results indicate that the seismic swarm was caused by activity on a two subfault network with different orientations. The results also show that aseismic slip on a southern subfault dominates the fault behaviour during a pre-M4.6 stage; after the aseismic pulse (during the most energetic stage), the largest event occurred on a northern subfault. Our results are consistent with an overlapping fault slip migration during the preM4.6 stage along the southern fault, followed by larger triggered coseismic ruptures of fault patches along the northern fault. Our model is consistent with small-scale spatially compact fault slip distribution and allows us to estimate lower bounds for the peak and average value of fault slip rates. These lower-bound estimates are consistent with reported values for slow slip events and other continental swarms.

The new inversion method presented here is complementary to the existing methodologies to estimate fault-slip distributions using geodetic data. We hope that this approach will be particularly useful with current and near-future multiconstellation InSAR satellite radar interferometry missions. In this near-future context, this tool could improve the identification of similar precursory (aseismic) slow slip during other long-lasting earthquake sequences (swarms), and help understand the driving mechanisms of earthquakes.

## Acknowledgments

This research was supported by the Natural Environmental Research Council (NERC) through the centre for the Observation and Modelling of Earthquakes, Volcanoes and Tectonics (UK) (GA/13/M/031) and the LiCS large grant (NE/K011006/1). This research was also supported by a Chinese Scholarship Council-University of Liverpool joint scholarship awarded to YJ (201706450071). PJG acknowledged the support of the Spanish Ministerio de Ciencia e Innovación research project, grant agreement number PID2019-104571RA-I00 (COMPACT) and the Beca Leonardo a Investigadores y Creadores Culturales 2020 from the Fundación BBVA. RADARSAT-2 images were acquired under SOARE project 28209 from the Canadian Space Agency, and ENVISAT images from ESA CAT1 project 6745. RADARSAT-2 and ENVISAT interferograms in the paper can be downloaded from <https://doi.org/10.5281/zenodo.5043161>. The finite-fault source model SRCMOD is retrieved from <http://equake-rc.info/srcmod/>. The geodetic inversion software slipBERI is retrieved from <https://github.com/ruthamey/slipBERI> and WGBIS package from <https://doi.org/10.5281/zenodo.3727158>. The CRUST 1.0 model

is retrieved from <https://igppweb.ucsd.edu/~gabi/crust1.html>. The manuscript was edited by Guido Jones, currently funded by the Cabildo de Tenerife, under the TFinnova Programme supported by MEDI and FDCAN funds. Thanks go to Mehdi Nikkhoo for providing the triangular dislocation functions for the displacement gradient tensor. The authors are also grateful to Tim Wright, Dan Faulkner, and Louisa Brotherson for insightful discussions of different aspects of this study, as well as to editor Rachel Abercrombie, associate editor, Eric Lindsey, and another anonymous reviewer for their helpful and constructive reviews, which greatly improved this manuscript.

## References

- Ainscoe, E. A., Elliott, J. R., Copley, A., Craig, T. J., Li, T., Parsons, B. E., & Walker, R. T. (2017). Blind Thrusting, Surface Folding, and the Development of Geological Structure in the Mw 6.3 2015 Pishan (China) Earthquake. *Journal of Geophysical Research: Solid Earth*, 122(11), 9359–9382. doi: 10.1002/2017JB014268
- Amey, R. M. J., Hooper, A., & Walters, R. J. (2018). A Bayesian Method for Incorporating Self-Similarity into Earthquake Slip Inversions. *Journal of Geophysical Research: Solid Earth*, 123(7), 6052–6071. doi: 10.1029/2017JB015316
- Argus, D. F., & Gordon, R. G. (1991). Current Sierra Nevada-North America motion from very long baseline interferometry: Implications for the kinematics of the western United States. *Geology*, 19(11), 1085–1088.
- Aster, R. C., Borchers, B., & Thurber, C. H. (2019). Chapter Three - Rank Deficiency and Ill-Conditioning. In R. C. Aster, B. Borchers, & C. H. Thurber (Eds.), *Parameter Estimation and Inverse Problems* (Third Edition ed., p. 55–91). Elsevier. doi: 10.1016/B978-0-12-804651-7.00008-0
- Bagnardi, M., & Hooper, A. (2018). Inversion of Surface Deformation Data for Rapid Estimates of Source Parameters and Uncertainties: A Bayesian Approach. *Geochemistry, Geophysics, Geosystems*, 19(7), 2194–2211. doi: 10.1029/2018GC007585
- Barnhart, W. D., Benz, H. M., Hayes, G. P., Rubinstein, J. L., & Bergman, E. (2014). Seismological and geodetic constraints on the 2011 Mw5.3 Trinidad, Colorado earthquake and induced deformation in the Raton Basin. *Journal of Geophysical Research: Solid Earth*, 119(10), 7923–7933. doi: 10.1002/2014JB011227
- Barnhart, W. D., & Lohman, R. B. (2010). Automated fault model discretization for inversions for coseismic slip distributions. *Journal of Geophysical Research: Solid Earth*, 115(B10). doi: 10.1029/2010JB007545
- Barnhart, W. D., Murray, J. R., Briggs, R. W., Gomez, F., Miles, C. P., Svarc, J., ... Stressler, B. J. (2016). Coseismic slip and early afterslip of the 2015 Illapel, Chile, earthquake: Implications for frictional heterogeneity and coastal uplift. *Journal of Geophysical Research: Solid Earth*, 121(8), 6172–6191. doi: 10.1002/2016JB013124

- Bedford, J., Moreno, M., Baez, J. C., Lange, D., Tilmann, F., Rosenau, M., ... Vigny, C. (2013). A high-resolution, time-variable afterslip model for the 2010 Maule Mw=8.8, Chile megathrust earthquake. *Earth and Planetary Science Letters*, 383, 26–36. doi: 10.1016/j.epsl.2013.09.020
- Bell, J. W., Amelung, F., & Henry, C. D. (2012). InSAR analysis of the 2008 Reno-Mogul earthquake swarm: Evidence for westward migration of Walker Lane style dextral faulting. *Geophysical Research Letters*, 39(18). doi: 10.1029/2012GL052795
- Bennett, R. A., Reilinger, R. E., Rodi, W., Yingping Li, Toksoz, M. N., & Hudnut, K. (1995). Coseismic fault slip associated with the 1992 Mw 6.1 Joshua Tree, California, earthquake: Implications for the Joshua Tree-Landers earthquake sequence. *Journal of Geophysical Research: Solid Earth*, 100(B4), 6443–6461. doi: 10.1029/94JB02944
- Bhattacharya, P., & Viesca, R. C. (2019). Fluid-induced aseismic fault slip outpaces pore-fluid migration. *Science*, 364(6439), 464–468. doi: 10.1126/science.aaw7354
- Biggs, J., Bergman, E., Emmerson, B., Funning, G. J., Jackson, J., Parsons, B., & Wright, T. J. (2006). Fault identification for buried strike-slip earthquakes using InSAR: The 1994 and 2004 Al Hoceima, Morocco earthquakes. *Geophysical Journal International*, 166(3), 1347–1362. doi: 10.1111/j.1365-246X.2006.03071.x
- Bletery, Q., & Nocquet, J. M. (2020). Slip bursts during coalescence of slow slip events in Cascadia. *Nature Communications*, 11(1), 1–6. doi: 10.1038/s41467-020-15494-4
- Bormann, J. M., Hammond, W. C., Kreemer, C., & Blewitt, G. (2016). Accommodation of missing shear strain in the Central Walker Lane, western North America: Constraints from dense GPS measurements. *Earth and Planetary Science Letters*, 440, 169–177. doi: 10.1016/j.epsl.2016.01.015
- Brune, J. N. (1970). Tectonic stress and the spectra of seismic shear waves from earthquakes. *Journal of Geophysical Research*, 75(26), 4997–5009. doi: 10.1029/JB075I026P04997
- Bürgmann, R., Ergintav, S., Segall, P., Hearn, E., McClusky, S., Reilinger, R., ... Zschau, J. (2002). Time-Dependent Distributed Afterslip on and Deep be-



- low the İzmit Earthquake Rupture. *Bulletin of the Seismological Society of America*, *92*, 126–137. doi: 10.1785/0120000833
- Caballero, E., Chounet, A., Duputel, Z., Jara, J., Twardzik, C., & Jolivet, R. (2021). Seismic and Aseismic Fault Slip During the Initiation Phase of the 2017 Mw=6.9 Valparaíso Earthquake. *Geophysical Research Letters*, *48*(6), e2020GL091916. doi: 10.1029/2020GL091916
- Cappa, F., Scuderi, M. M., Collettini, C., Guglielmi, Y., & Avouac, J. P. (2019). Stabilization of fault slip by fluid injection in the laboratory and in situ. *Science Advances*, *5*(3), eaau4065. doi: 10.1126/sciadv.aau4065
- Cattania, C., & Segall, P. (2021). Precursory slow slip and foreshocks on rough faults. *Journal of Geophysical Research: Solid Earth*, e2020JB020430. doi: 10.1029/2020JB020430
- Champenois, J., Baize, S., Vallee, M., Jomard, H., Alvarado, A., Espin, P., ... Audin, L. (2017). Evidences of Surface Rupture Associated with a Low-Magnitude (Mw 5.0) Shallow Earthquake in the Ecuadorian Andes. *Journal of Geophysical Research: Solid Earth*, *122*(10), 8446–8458. doi: 10.1002/2017JB013928
- Cheloni, D., D’Agostino, N., Selvaggi, G., Avallone, A., Fornaro, G., Giuliani, R., ... Tizzani, P. (2017). Aseismic transient during the 2010-2014 seismic swarm: Evidence for longer recurrence of  $M \geq 6.5$  earthquakes in the Pollino gap (Southern Italy)? *Scientific Reports*, *7*(1), 1–10. doi: 10.1038/s41598-017-00649-z
- Ciardo, F., & Lecampion, B. (2019). Effect of Dilatancy on the Transition from Aseismic to Seismic Slip Due to Fluid Injection in a Fault. *Journal of Geophysical Research: Solid Earth*, *124*(4), 3724–3743. doi: 10.1029/2018JB016636
- De Barros, L., Cappa, F., Deschamps, A., & Dublanchet, P. (2020). Imbricated Aseismic Slip and Fluid Diffusion Drive a Seismic Swarm in the Corinth Gulf, Greece. *Geophysical Research Letters*, *47*(9). doi: 10.1029/2020GL087142
- Delorey, A. A., van der Elst, N. J., & Johnson, P. A. (2017). Tidal triggering of earthquakes suggests poroelastic behavior on the San Andreas Fault. *Earth and Planetary Science Letters*, *460*, 164–170. doi: 10.1016/j.epsl.2016.12.014
- Di Carli, S., François-Holden, C., Peyrat, S., & Madariaga, R. (2010). Dynamic inversion of the 2000 Tottori earthquake based on elliptical subfault ap-

- proximations. *Journal of Geophysical Research*, 115(B12), B12328. doi:  
10.1029/2009JB006358
- Dodge, D. A., Beroza, G. C., & Ellsworth, W. L. (1996). Detailed observations of  
California foreshock sequences: Implications for the earthquake initiation pro-  
cess. *Journal of Geophysical Research: Solid Earth*, 101(B10), 22371–22392.  
doi: 10.1029/96JB02269
- Du, Y., Aydin, A., & Segall, P. (1992). Comparison of various inversion techniques  
as applied to the determination of a geophysical deformation model for the  
1983 Borah Peak earthquake. *Bulletin of the Seismological Society of America*,  
82(4), 1840–1866.
- Elliott, J. R., Walters, R. J., England, P. C., Jackson, J. A., Li, Z., & Parsons, B.  
(2010). Extension on the Tibetan plateau: recent normal faulting measured by  
InSAR and body wave seismology. *Geophysical Journal International*, 183(2),  
503–535. doi: 10.1111/j.1365-246X.2010.04754.x
- Engwirda, D. (2014). *Locally optimal Delaunay-refinement and optimisation-based  
mesh generation* (Doctoral dissertation, University of Sydney). Retrieved from  
<http://hdl.handle.net/2123/13148>
- Faulds, J., & Henry, C. (2008). Tectonic influences on the spatial and temporal  
evolution of the Walker Lane: An incipient transform fault along the evolving  
Pacific - North American plate boundary. *Arizona Geological Society Digest*,  
22, 437–470.
- Floyd, M. A., Walters, R. J., Elliott, J. R., Funning, G. J., Svarc, J. L., Murray,  
J. R., ... Wright, T. J. (2016). Spatial variations in fault friction related  
to lithology from rupture and afterslip of the 2014 South Napa, Califor-  
nia, earthquake. *Geophysical Research Letters*, 43(13), 6808–6816. doi:  
10.1002/2016GL069428
- Fukahata, Y., & Wright, T. J. (2008). A non-linear geodetic data inversion using  
ABIC for slip distribution on a fault with an unknown dip angle. *Geophysical  
Journal International*, 173(2), 353–364. doi: 10.1111/j.1365-246X.2007.03713  
.x
- Fukuda, J. (2018). Variability of the Space-Time Evolution of Slow Slip Events Off  
the Boso Peninsula, Central Japan, From 1996 to 2014. *Journal of Geophysical  
Research: Solid Earth*, 123(1), 732–760. doi: 10.1002/2017JB014709

- 862 Fukuda, J., & Johnson, K. M. (2008). A fully Bayesian inversion for spatial distri-  
 863 bution of fault slip with objective smoothing. *Bulletin of the Seismological So-*  
 864 *ciety of America*, 98(3), 1128–1146. doi: 10.1785/0120070194
- 865 Fukuda, J., & Johnson, K. M. (2010). Mixed linear-non-linear inversion of crustal  
 866 deformation data: Bayesian inference of model, weighting and regularization  
 867 parameters. *Geophysical Journal International*, 181(3), 1441–1458. doi:  
 868 10.1111/j.1365-246X.2010.04564.x
- 869 Gavish, M., & Donoho, D. L. (2014). The optimal hard threshold for singular values  
 870 is  $4/\sqrt{3}$ . *IEEE Transactions on Information Theory*, 60(8), 5040–5053. doi: 10  
 871 .1109/TIT.2014.2323359
- 872 Gomberg, J. (2018). Unsettled earthquake nucleation. *Nature Geoscience*, 11(7),  
 873 463–464. doi: 10.1038/s41561-018-0149-x
- 874 Gomberg, J., & Johnson, P. (2005). Dynamic triggering of earthquakes. *Nature*,  
 875 437(7060), 830. doi: 10.1038/437830a
- 876 González, P. J., Samsonov, S. V., Pepe, S., Tiampo, K. F., Tizzani, P., Casu, F., ...  
 877 Sansosti, E. (2013). Magma storage and migration associated with the 2011-  
 878 2012 El Hierro eruption: Implications for crustal magmatic systems at oceanic  
 879 island volcanoes. *Journal of Geophysical Research: Solid Earth*, 118(8), 4361–  
 880 4377. doi: 10.1002/jgrb.50289
- 881 Grandin, R., Socquet, A., Doin, M.-P., Jacques, E., de Chabaliér, J.-B., & King,  
 882 G. C. P. (2010). Transient rift opening in response to multiple dike injec-  
 883 tions in the Manda Hararo rift (Afar, Ethiopia) imaged by time-dependent  
 884 elastic inversion of interferometric synthetic aperture radar data. *Journal of*  
 885 *Geophysical Research*, 115(B9), B09403. doi: 10.1029/2009JB006883
- 886 Gualandi, A., Nichele, C., Serpelloni, E., Chiaraluce, L., Anderlini, L., Latorre, D.,  
 887 ... Avouac, J.-P. (2017). Aseismic deformation associated with an earth-  
 888 quake swarm in the northern Apennines (Italy). *Geophysical Research Letters*,  
 889 44(15), 7706–7714. doi: 10.1002/2017GL073687
- 890 Guglielmi, Y., Cappa, F., Avouac, J. P., Henry, P., & Elsworth, D. (2015). Seismic-  
 891 ity triggered by fluid injection-induced aseismic slip. *Science*, 348(6240), 1224–  
 892 1226. doi: 10.1126/science.aab0476
- 893 Hamling, I. J., Hreinsdóttir, S., Clark, K., Elliott, J., Liang, C., Fielding, E.,  
 894 ... Stirling, M. (2017). Complex multifault rupture during the 2016

- 895 Mw 7.8 Kaikōura earthquake, New Zealand. *Science*, *356*(6334). doi:  
 896 10.1126/science.aam7194
- 897 Hammond, W. C., & Thatcher, W. (2007). Crustal deformation across the Sierra  
 898 Nevada, northern Walker Lane, Basin and Range transition, western United  
 899 States measured with GPS, 2000–2004. *Journal of Geophysical Research: Solid*  
 900 *Earth*, *112*(B5), 5411. doi: 10.1029/2006JB004625
- 901 Harris, R. A., & Segall, P. (1987). Detection of a locked zone at depth on the Park-  
 902 field, California, segment of the San Andreas Fault. *Journal of Geophysical Re-*  
 903 *search*, *92*(B8), 7945. doi: 10.1029/JB092iB08p07945
- 904 Hatch, R. L., Abercrombie, R. E., Ruhl, C. J., & Smith, K. D. (2018). Earth-  
 905 quake Interaction, Fault Structure, and Source Properties of a Small Sequence  
 906 in 2017 near Truckee, CaliforniaEarthquake Interaction, Fault Structure,  
 907 and Source Properties of a Small Sequence in 2017 near Truckee. *Bul-*  
 908 *letin of the Seismological Society of America*, *108*(5A), 2580–2593. doi:  
 909 10.1785/0120180089
- 910 Hatch, R. L., Abercrombie, R. E., Ruhl, C. J., & Smith, K. D. (2020). Evidence of  
 911 Aseismic and Fluid-Driven Processes in a Small Complex Seismic Swarm Near  
 912 Virginia City, Nevada. *Geophysical Research Letters*, *47*(4), e2019GL085477.  
 913 doi: 10.1029/2019GL085477
- 914 Hatch-Ibarra, R. L., Abercrombie, R. E., Ruhl, C. J., Smith, K. D., Hammond,  
 915 W. C., & Pierce, I. K. (2022). The 2016 Nine Mile Ranch Earthquakes:  
 916 Hazard and Tectonic Implications of Orthogonal Conjugate Faulting in  
 917 the Walker Lane. *Bulletin of the Seismological Society of America*. doi:  
 918 10.1785/0120210149
- 919 Hicks, S. P., Okuwaki, R., Steinberg, A., Rychert, C. A., Harmon, N., Abercrombie,  
 920 R. E., ... Sudhaus, H. (2020). Back-propagating supershear rupture in the  
 921 2016 Mw 7.1 Romanche transform fault earthquake. *Nature Geoscience*, *13*(9),  
 922 647–653. doi: 10.1038/s41561-020-0619-9
- 923 Hinz, N., Faulds, J., Moeck, I., Bell, J. W., & Oldow, J. S. (2010). Structural con-  
 924 trols of three blind geothermal resources at the hawthorne ammunition depot,  
 925 West-Central Nevada. *Transactions - Geothermal Resources Council*, *34*,  
 926 720–725.
- 927 Hirose, H., & Obara, K. (2010). Recurrence behavior of short-term slow slip

- 928 and correlated nonvolcanic tremor episodes in western Shikoku, southwest  
 929 Japan. *Journal of Geophysical Research: Solid Earth*, 115(B6), 0–21. doi:  
 930 10.1029/2008JB006050
- 931 Houston, H., Delbridge, B. G., Wech, A. G., & Creager, K. C. (2011). Rapid tremor  
 932 reversals in Cascadia generated by a weakened plate interface. *Nature Geo-*  
 933 *science*, 4(6), 404–409. doi: 10.1038/ngeo1157
- 934 Hussain, E., Hooper, A., Wright, T. J., Walters, R. J., & Bekaert, D. P. (2016).  
 935 Interseismic strain accumulation across the central North Anatolian Fault from  
 936 iteratively unwrapped InSAR measurements. *Journal of Geophysical Research:*  
 937 *Solid Earth*, 121(12), 9000–9019. doi: 10.1002/2016JB013108
- 938 Ichinose, G. A., Anderson, J. G., Smith, K. D., & Zeng, Y. (2003). Source Param-  
 939 eters of Eastern California and Western Nevada Earthquakes from Regional  
 940 Moment Tensor Inversion. *Bulletin of the Seismological Society of America*,  
 941 93(1), 61–84. doi: 10.1785/0120020063
- 942 Ingleby, T., Wright, T. J., Hooper, A., Craig, T. J., & Elliott, J. R. (2020). Con-  
 943 straints on the Geometry and Frictional Properties of the Main Himalayan  
 944 Thrust Using Coseismic, Postseismic, and Interseismic Deformation in Nepal.  
 945 *Journal of Geophysical Research: Solid Earth*, 125(2), e2019JB019201. doi:  
 946 10.1029/2019JB019201
- 947 Jiang, Y., & González, P. J. (2020). Bayesian Inversion of Wrapped Satellite  
 948 Interferometric Phase to Estimate Fault and Volcano Surface Ground Defor-  
 949 mation Models. *Journal of Geophysical Research: Solid Earth*, 125(5). doi:  
 950 10.1029/2019JB018313
- 951 Jiang, Y., & González, P. J. (2021). High-resolution spatio-temporal fault slip using  
 952 InSAR observations: insights on seismic and aseismic slip during a shallow  
 953 crust earthquake swarm. In *EGU General Assembly Conference Abstracts*. doi:  
 954 10.5194/egusphere-egu21-6280
- 955 Jiang, Y., González, P. J., & Bürgmann, R. (2022). Subduction earthquakes con-  
 956 trolled by incoming plate geometry: The 2020  $M > 7.5$  Shumagin, Alaska,  
 957 earthquake doublet. *Earth and Planetary Science Letters*, 584, 117447. doi:  
 958 10.1016/J.EPSL.2022.117447
- 959 Johanson, I. A., & Bürgmann, R. (2005). Creep and quakes on the northern tran-  
 960 sition zone of the San Andreas fault from GPS and InSAR data. *Geophysical*

- 961 *Research Letters*, 32(14), 1–5. doi: 10.1029/2005GL023150
- 962 Johnson, K. M., Fukuda, J., & Segall, P. (2012). Challenging the rate-state as-  
 963 perity model: Afterslip following the 2011 M9 Tohoku-oki, Japan, earth-  
 964 quake. *Geophysical Research Letters*, 39(20), 2012GL052901. doi:  
 965 10.1029/2012GL052901
- 966 Jolivet, R., Lasserre, C., Doin, M. P., Guillaso, S., Peltzer, G., Dailu, R., . . . Xu, X.  
 967 (2012). Shallow creep on the Haiyuan Fault (Gansu, China) revealed by SAR  
 968 Interferometry. *Journal of Geophysical Research: Solid Earth*, 117(B6), 6401.  
 969 doi: 10.1029/2011JB008732
- 970 Kampes, B., Hanssen, R., & Perski, Z. (2003). Radar interferometry with public do-  
 971 main tools. *Proc. of FRINGE 2003 Workshop*.
- 972 Kaneko, Y., & Shearer, P. M. (2014). Seismic source spectra and estimated stress  
 973 drop derived from cohesive-zone models of circular subshear rupture. *Geophys-  
 974 ical Journal International*, 197(2), 1002–1015. doi: 10.1093/gji/ggu030
- 975 Ke, C.-Y., McLaskey, G. C., & Kammer, D. S. (2020). The Earthquake Arrest Zone.  
 976 *Geophysical Journal International*. doi: 10.1093/gji/ggaa386
- 977 Khoshmanesh, M., Shirzaei, M., & Nadeau, R. M. (2015). Time-dependent model  
 978 of aseismic slip on the central San Andreas Fault from InSAR time series and  
 979 repeating earthquakes. *Journal of Geophysical Research: Solid Earth*, 120(9),  
 980 6658–6679. doi: 10.1002/2015JB012039
- 981 King, G. C. P., Stein, R. S., & Lin, J. (1994). Static stress changes and the trig-  
 982 gering of earthquakes. *Bulletin of the Seismological Society of America*, 84(3),  
 983 935–953.
- 984 Klein, E., Duputel, Z., Zigone, D., Vigny, C., Boy, J.-P., Doubre, C., & Meneses,  
 985 G. (2018). Deep transient slow slip detected by survey gps in the region of  
 986 atacama, chile. *Geophysical Research Letters*, 45(22), 12,263–12,273. doi:  
 987 10.1029/2018GL080613
- 988 Kreemer, C., Blewitt, G., & Hammond, W. C. (2009). Geodetic constraints on  
 989 contemporary deformation in the northern Walker Lane: 2. Velocity and  
 990 strain rate tensor analysis. In *Late Cenozoic Structure and Evolution of the  
 991 Great Basin-Sierra Nevada Transition*. Geological Society of America. doi:  
 992 10.1130/2009.2447(02)
- 993 Kreemer, C., Blewitt, G., & Klein, E. C. (2014). A geodetic plate motion and Global

- 994 Strain Rate Model. *Geochemistry, Geophysics, Geosystems*, 15(10), 3849–3889.  
 995 doi: 10.1002/2014GC005407
- 996 Kyriakopoulos, C., Chini, M., Bignami, C., Stramondo, S., Ganas, A., Kolligri, M.,  
 997 & Moshou, A. (2013). Monthly migration of a tectonic seismic swarm detected  
 998 by DInSAR: Southwest Peloponnese, Greece. *Geophysical Journal Interna-*  
 999 *tional*, 194(3), 1302–1309. doi: 10.1093/gji/ggt196
- 1000 Lambert, V., Lapusta, N., & Perry, S. (2021). Propagation of large earthquakes as  
 1001 self-healing pulses or mild cracks. *Nature*, 591(7849), 252–258. doi: 10.1038/  
 1002 s41586-021-03248-1
- 1003 Lange, R. A., & Carmichael, I. S. E. (1996). The Aurora volcanic field, California-  
 1004 Nevada: oxygen fugacity constraints on the development of andesitic  
 1005 magma. *Contributions to Mineralogy and Petrology*, 125(2), 167–185. doi:  
 1006 10.1007/s004100050214
- 1007 Liu, Y., McGuire, J. J., & Behn, M. D. (2020). Aseismic transient slip on the Go-  
 1008 far transform fault, East Pacific Rise. *Proceedings of the National Academy of*  
 1009 *Sciences of the United States of America*, 117(19), 10188–10194. doi: 10.1073/  
 1010 pnas.1913625117
- 1011 Lohman, R. B., & McGuire, J. J. (2007). Earthquake swarms driven by aseismic  
 1012 creep in the Salton Trough, California. *Journal of Geophysical Research: Solid*  
 1013 *Earth*, 112(4). doi: 10.1029/2006JB004596
- 1014 Luo, Y., & Liu, Z. (2019). Rate-and-State Model Casts New Insight into Episodic  
 1015 Tremor and Slow-slip Variability in Cascadia. *Geophysical Research Letters*,  
 1016 46(12), 6352–6362. doi: 10.1029/2019GL082694
- 1017 Madariaga, R. (1976). Dynamics of an expanding circular fault. *Bulletin of the Seis-*  
 1018 *mological Society of America*, 66(3), 639–666.
- 1019 Mai, P. M., & Beroza, G. C. (2002). A spatial random field model to characterize  
 1020 complexity in earthquake slip. *Journal of Geophysical Research: Solid Earth*,  
 1021 107(B11), ESE 10–1–ESE 10–21. doi: 10.1029/2001jb000588
- 1022 Mai, P. M., & Thingbaijam, K. K. (2014). SRCMOD: An online database of finite-  
 1023 fault rupture models. *Seismological Research Letters*, 85(6), 1348–1357. doi:  
 1024 10.1785/0220140077
- 1025 Marone, C., & Richardson, E. (2006). Do earthquakes rupture piece by piece or all  
 1026 together? *Science*, 313(5794), 1748–1749. doi: 10.1126/science.1131296

- 1027 Matthews, M. V., & Segall, P. (1993). Estimation of depth-dependent fault slip  
1028 from measured surface deformation with application to the 1906 San Francisco  
1029 earthquake. *Journal of Geophysical Research*, 98(B7), 12153–12163. doi:  
1030 10.1029/93jb00440
- 1031 Mesimeri, M., & Karakostas, V. (2018). Repeating earthquakes in western Corinth  
1032 Gulf (Greece): Implications for aseismic slip near locked faults. *Geophysical*  
1033 *Journal International*, 215(1), 659–676. doi: 10.1093/gji/ggy301
- 1034 Michel, S., Gualandi, A., & Avouac, J. P. (2019). Similar scaling laws for earth-  
1035 quakes and Cascadia slow-slip events. *Nature*, 574(7779), 522–526. doi: 10  
1036 .1038/s41586-019-1673-6
- 1037 Minson, S. E., Simons, M., & Beck, J. L. (2013). Bayesian inversion for finite fault  
1038 earthquake source models I—theory and algorithm. *Geophysical Journal Inter-*  
1039 *national*, 194(3), 1701–1726. doi: 10.1093/gji/ggt180
- 1040 Mori, J. (1996). Rupture directivity and slip distribution of the M 4.3 foreshock to  
1041 the 1992 Joshua Tree earthquake, Southern California. *Bulletin of the Seismo-*  
1042 *logical Society of America*, 86(3), 805–810. doi: 10.1785/BSSA0860030805
- 1043 Nadeau, R. M., & McEvilly, T. V. (1999). Fault slip rates at depth from recurrence  
1044 intervals of repeating microearthquakes. *Science*, 285(5428), 718–721. doi: 10  
1045 .1126/science.285.5428.718
- 1046 Nissen, E., Ghorashi, M., Jackson, J., Parsons, B., & Talebian, M. (2007). The  
1047 2005 Qeshm Island earthquake (Iran) - A link between buried reverse faulting  
1048 and surface folding in the Zagros Simply Folded Belt? *Geophysical Journal*  
1049 *International*, 171(1), 326–338. doi: 10.1111/j.1365-246X.2007.03514.x
- 1050 Ozawa, S., Yarai, H., & Kobayashi, T. (2019). Recovery of the recurrence interval of  
1051 Boso slow slip events in Japan. *Earth, Planets and Space*, 71(1), 1–8. doi: 10  
1052 .1186/s40623-019-1058-y
- 1053 Parotidis, M., Rothert, E., & Shapiro, S. A. (2003). Pore-pressure diffu-  
1054 sion: A possible triggering mechanism for the earthquake swarms 2000 in  
1055 Vogtland/NW-Bohemia, central Europe. *Geophysical Research Letters*, 30(20),  
1056 2003GL018110. doi: 10.1029/2003GL018110
- 1057 Passarelli, L., Rivalta, E., Jónsson, S., Hensch, M., Metzger, S., Jakobsdóttir, S. S.,  
1058 ... Dahm, T. (2018). Scaling and spatial complementarity of tectonic  
1059 earthquake swarms. *Earth and Planetary Science Letters*, 482, 62–70. doi:



- 10.1016/j.epsl.2017.10.052
- Pritchard, M. E., & Simons, M. (2006). An aseismic slip pulse in northern Chile and along-strike variations in seismogenic behavior. *Journal of Geophysical Research: Solid Earth*, 111(8). doi: 10.1029/2006JB004258
- Radiguet, M., Cotton, F., Vergnolle, M., Campillo, M., Valette, B., Kostoglodov, V., & Cotte, N. (2011). Spatial and temporal evolution of a long term slow slip event: the 2006 Guerrero Slow Slip Event. *Geophysical Journal International*, 184(2), 816–828. doi: 10.1111/j.1365-246X.2010.04866.x
- Radiguet, M., Perfettini, H., Cotte, N., Gualandi, A., Valette, B., Kostoglodov, V., ... Campillo, M. (2016). Triggering of the 2014 Mw7.3 Papanao earthquake by a slow slip event in Guerrero, Mexico. *Nature Geoscience* 2016 9:11, 9(11), 829–833. doi: 10.1038/ngeo2817
- Ragon, T., Sladen, A., & Simons, M. (2018). Accounting for uncertain fault geometry in earthquake source inversions – I: theory and simplified application. *Geophysical Journal International*, 214(2), 1174–1190. doi: 10.1093/gji/ggy187
- Romanet, P., Bhat, H. S., Jolivet, R., & Madariaga, R. (2018). Fast and Slow Slip Events Emerge Due to Fault Geometrical Complexity. *Geophysical Research Letters*, 45(10), 4809–4819. doi: 10.1029/2018GL077579
- Rousset, B., Fu, Y., Bartlow, N., & Bürgmann, R. (2019). Weeks-Long and Years-Long Slow Slip and Tectonic Tremor Episodes on the South Central Alaska Megathrust. *Journal of Geophysical Research: Solid Earth*, 124(12), 13392–13403. doi: 10.1029/2019JB018724
- Ruhl, C. J., Abercrombie, R. E., Smith, K. D., & Zaliapin, I. (2016). Complex spatiotemporal evolution of the 2008 Mw 4.9 Mogul earthquake swarm (Reno, Nevada): Interplay of fluid and faulting. *Journal of Geophysical Research: Solid Earth*, 121(11), 8196–8216. doi: 10.1002/2016JB013399
- Ruhl, C. J., Morton, E. A., Bormann, J. M., Hatch-Ibarra, R., Ichinose, G., & Smith, K. D. (2021). Complex Fault Geometry of the 2020 Mww 6.5 Monte Cristo Range, Nevada, Earthquake Sequence. *Seismological Research Letters*, 92, 1876-1890. doi: 10.1785/02202000345
- Salman, R., Hill, E. M., Feng, L., Lindsey, E. O., Mele Veedu, D., Barbot, S., ... Natawidjaja, D. H. (2017). Piecemeal Rupture of the Mentawai Patch, Sumatra: The 2008 Mw 7.2 North Pagai Earthquake Sequence. *Journal of Geophys-*

- ical Research: Solid Earth, 122(11), 9404–9419. doi: 10.1002/2017JB014341
- Samsonov, S., & D’Orey, N. (2012). Multidimensional time-series analysis of ground deformation from multiple InSAR data sets applied to Virunga Volcanic Province. *Geophysical Journal International*, 191(3), 1095–1108. doi: 10.1111/j.1365-246X.2012.05669.x
- Schmidt, D. A., Bürgmann, R., Nadeau, R. M., & D’Alessio, M. (2005). Distribution of aseismic slip rate on the Hayward fault inferred from seismic and geodetic data. *Journal of Geophysical Research: Solid Earth*, 110(B8), 1–15. doi: 10.1029/2004JB003397
- Scott, C., Bunds, M., Shirzaei, M., & Toke, N. (2020). Creep Along the Central San Andreas Fault From Surface Fractures, Topographic Differencing, and InSAR. *Journal of Geophysical Research: Solid Earth*, 125(10), e2020JB019762. doi: 10.1029/2020JB019762
- Segall, P., & Rice, J. R. (1995). Dilatancy, compaction, and slip instability of a fluid-infiltrated fault. *Journal of Geophysical Research: Solid Earth*, 100(B11), 22155–22171. doi: 10.1029/95JB02403
- Segall, P., Rubin, A. M., Bradley, A. M., & Rice, J. R. (2010). Dilatant strengthening as a mechanism for slow slip events. *Journal of Geophysical Research*, 115(B12), B12305. doi: 10.1029/2010JB007449
- Shearer, P. M., Prieto, G. A., & Hauksson, E. (2006). Comprehensive analysis of earthquake source spectra in southern California. *Journal of Geophysical Research: Solid Earth*, 111(B6), 6303. doi: 10.1029/2005JB003979
- Shen, Z. K., Sun, J., Zhang, P., Wan, Y., Wang, M., Bürgmann, R., . . . Wang, Q. (2009). Slip maxima at fault junctions and rupturing of barriers during the 2008 Wenchuan earthquake. *Nature Geoscience*, 2(10), 718–724. doi: 10.1038/ngeo636
- Smith, K., Johnson, C., Davies, J., Agbaje, T., Knezevic Antonijevic, S., & Kent, G. (2011). The 2011 Hawthorne, Nevada, Earthquake Sequence: Shallow Normal Faulting. In *AGU Fall Meeting* (pp. S53B–2284).
- Song, X., Jiang, Y., Shan, X., Gong, W., & Qu, C. (2019). A Fine Velocity and Strain Rate Field of Present-Day Crustal Motion of the Northeastern Tibetan Plateau Inverted Jointly by InSAR and GPS. *Remote Sensing 2019, Vol. 11, Page 435*, 11(4), 435. doi: 10.3390/RS11040435

- 1126 Stein, S., & Gordon, R. G. (1984). Statistical tests of additional plate boundaries  
1127 from plate motion inversions. *Earth and Planetary Science Letters*, 69(2), 401–  
1128 412. doi: 10.1016/0012-821X(84)90198-5
- 1129 Sun, J., Johnson, K. M., Cao, Z., Shen, Z., Bürgmann, R., & Xu, X. (2011). Me-  
1130 chanical constraints on inversion of coseismic geodetic data for fault slip and  
1131 geometry: Example from InSAR observation of the 6 October 2008 Mw 6.3  
1132 Dangxiong-Yangyi (Tibet) earthquake. *Journal of Geophysical Research*,  
1133 116(B1), B01406. doi: 10.1029/2010JB007849
- 1134 Takenaka, H., & Fujii, Y. (2008). A compact representation of spatio-temporal slip  
1135 distribution on a rupturing fault. *Journal of Seismology*, 12, 281-293. doi: 10  
1136 .1007/s10950-007-9087-6
- 1137 Taymaz, T., Wright, T. J., Yolsal, S., Tan, O., Fielding, E., & Seyitoğlu, G. (2007).  
1138 Source characteristics of the 6 June 2000 Orta-Çankiri (central Turkey) earth-  
1139 quake: A synthesis of seismological, geological and geodetic (InSAR) obser-  
1140 vations, and internal deformation of the Anatolian plate. *Geological Society*  
1141 *Special Publication*, 291(1), 259–290. doi: 10.1144/SP291.12
- 1142 Thatcher, W., Foulger, G. R., Julian, B. R., Svarc, J., Quilty, E., & Bawden,  
1143 G. W. (1999, 3). Present-day deformation across the basin and range  
1144 province, western united states. *Science*, 283, 1714-1718. doi: 10.1126/  
1145 SCIENCE.283.5408.1714
- 1146 Thomas, M. Y., Avouac, J.-P., Champenois, J., Lee, J.-C., Kuo, L.-C., Thomas,  
1147 M. Y., ... Kuo, L.-C. (2014). Spatiotemporal evolution of seismic and aseis-  
1148 mic slip on the Longitudinal Valley Fault, Taiwan. *Journal of Geophysical*  
1149 *Research: Solid Earth*, 119(6), 5114–5139. doi: 10.1002/2013JB010603
- 1150 Tridon, M., Cayol, V., Froger, J., Augier, A., & Bachèlery, P. (2016). Inversion of co-  
1151 eval shear and normal stress of Piton de la Fournaise flank displacement. *Jour-  
1152 nal of Geophysical Research: Solid Earth*, 121(11), 7846–7866. doi: 10.1002/  
1153 2016JB013330
- 1154 Tsang, L. L. H., Hill, E. M., Barbot, S., Qiu, Q., Feng, L., Hermawan, I., ... Nataw-  
1155 idjaja, D. H. (2016). Afterslip following the 2007 Mw 8.4 Bengkulu earthquake  
1156 in Sumatra loaded the 2010 Mw 7.8 Mentawai tsunami earthquake rupture  
1157 zone. *Journal of Geophysical Research: Solid Earth*, 121(12), 9034–9049. doi:  
1158 10.1002/2016JB013432

- 1159 Turner, R. C., Nadeau, R. M., & Bürgmann, R. (2013). Aseismic slip and fault in-  
 1160 teraction from repeating earthquakes in the Loma Prieta aftershock zone. *Geo-*  
 1161 *physical Research Letters*, 40(6), 1079–1083. doi: 10.1002/grl.50212
- 1162 Uchide, T., Shearer, P. M., & Imanishi, K. (2014). Stress drop variations among  
 1163 small earthquakes before the 2011 Tohoku-oki, Japan, earthquake and impli-  
 1164 cations for the main shock. *Journal of Geophysical Research: Solid Earth*,  
 1165 119(9), 7164–7174. doi: 10.1002/2014JB010943
- 1166 Villegas-Lanza, J. C., Nocquet, J. M., Rolandone, F., Vallee, M., Tavera, H., Bon-  
 1167 doux, F., ... Chlieh, M. (2016). A mixed seismic-aseismic stress release  
 1168 episode in the Andean subduction zone. *Nature Geoscience*, 9(2), 150–154.  
 1169 doi: 10.1038/ngeo2620
- 1170 Wallace, L. M. (2020). Slow Slip Events in New Zealand. *Annual Review of Earth*  
 1171 *and Planetary Sciences*, 48(1), 175–203. doi: 10.1146/annurev-earth-071719-  
 1172 -055104
- 1173 Wallace, L. M., Beavan, J., Bannister, S., & Williams, C. (2012). Simultaneous long-  
 1174 term and short-term slow slip events at the Hikurangi subduction margin, New  
 1175 Zealand: Implications for processes that control slow slip event occurrence,  
 1176 duration, and migration. *Journal of Geophysical Research B: Solid Earth*,  
 1177 117(11). doi: 10.1029/2012JB009489
- 1178 Walters, R. J., Elliott, J. R., D’Agostino, N., England, P. C., Hunstad, I., Jackson,  
 1179 J. A., ... Roberts Edinburgh, G. (2009). The 2009 L’Aquila earthquake  
 1180 (central Italy): A source mechanism and implications for seismic hazard. *Geo-*  
 1181 *physical Research Letters*, 36(17). doi: 10.1029/2009GL039337
- 1182 Wech, A. G., Creager, K. C., & Melbourne, T. I. (2009). Seismic and geodetic con-  
 1183 straints on Cascadia slow slip. *Journal of Geophysical Research: Solid Earth*,  
 1184 114(10). doi: 10.1029/2008JB006090
- 1185 Werner, C. (2000). GAMMA SAR and interferometric processing software. *Proceed-*  
 1186 *ings of ERS-Envisat Symposium ; 16-20 October, Gothenburg, Sweden, 2000*.
- 1187 Wesnousky, S. (2005). Active faulting in the Walker Lane. *Tectonics*, 24(3). doi: 10  
 1188 .1029/2004TC001645
- 1189 Wicks, C., Thelen, W., Weaver, C., Gomberg, J., Rohay, A., & Bodin, P. (2011).  
 1190 InSAR observations of aseismic slip associated with an earthquake swarm in  
 1191 the Columbia River flood basalts. *Journal of Geophysical Research*, 116(B12),

- 1192 B12304. doi: 10.1029/2011JB008433
- 1193 Xu, W., Bürgmann, R., & Li, Z. (2016). An improved geodetic source model for the  
 1194 1999 Mw 6.3 Chamoli earthquake, India. *Geophysical Journal International*,  
 1195 *205*(1), 236–242. doi: 10.1093/gji/ggw016
- 1196 Yamashita, Y., Yakiwara, H., Asano, Y., Shimizu, H., Uchida, K., Hirano, S., ...  
 1197 Obara, K. (2015). Migrating tremor off southern Kyushu as evidence for  
 1198 slow slip of a shallow subduction interface. *Science*, *348*(6235), 676–679. doi:  
 1199 10.1126/science.aaa4242
- 1200 Zha, X., Jia, Z., Dai, Z., & Lu, Z. (2019). The cause of the 2011 Hawthorne  
 1201 (Nevada) earthquake swarm constrained by seismic and InSAR methods.  
 1202 *Journal of Geodesy*, *93*(6), 899–909. doi: 10.1007/s00190-018-1212-5

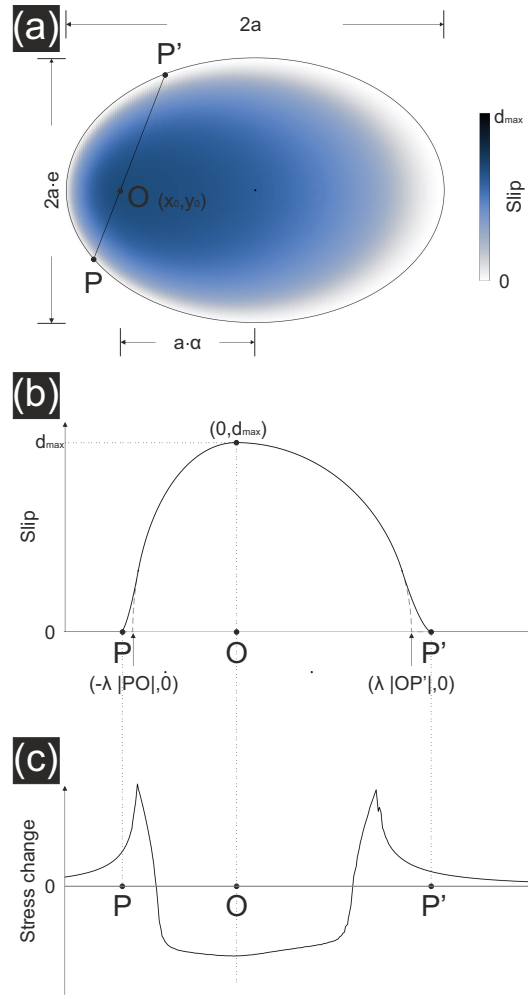


**Figure 1.** Parameters of the proposed slip model. Image (a) shows the 2d slip distribution, with an elliptical shape. The slip and stress changes along profile  $POP'$  are presented in images (b)-(c).

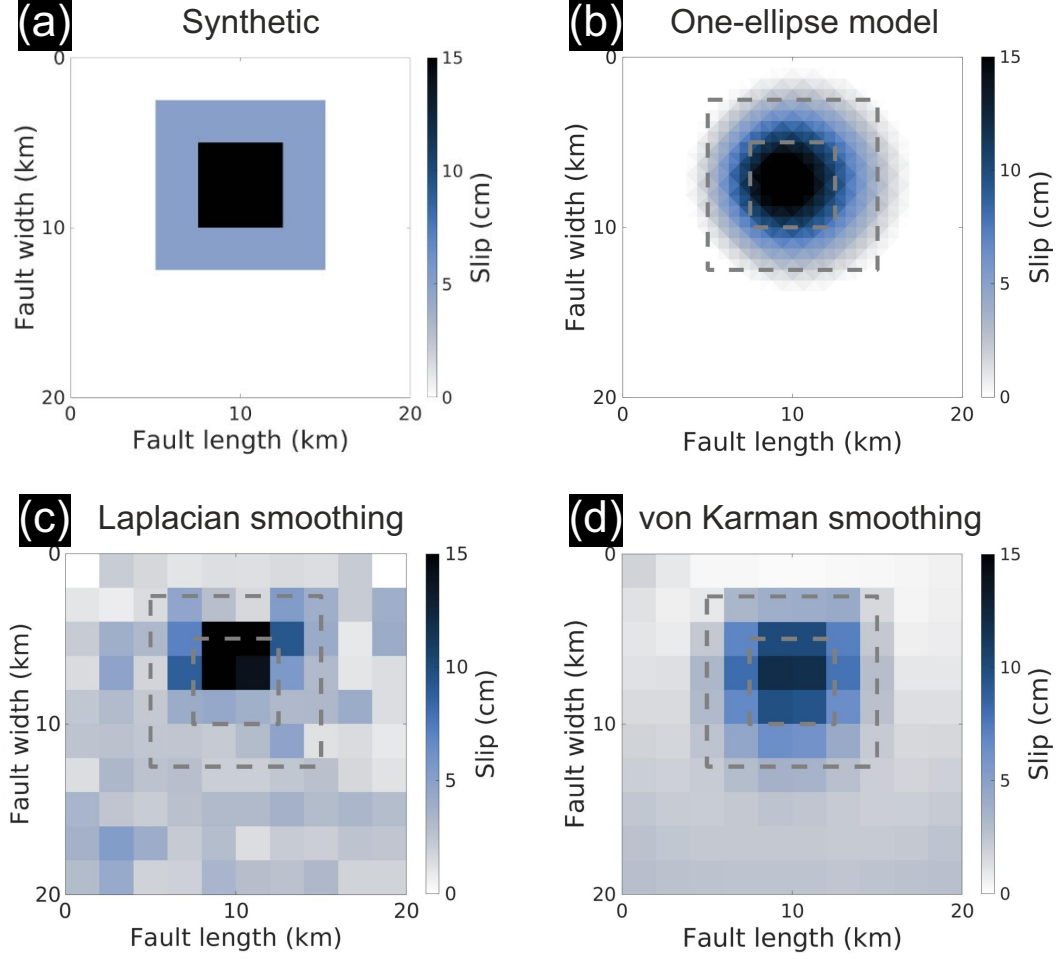


**Figure 2.** Synthetic and modelled fault slip distribution for a synthetic case. Image (a) shows the synthetic non-uniform slip distribution on a simulated fault plane. The black area is a  $5 \text{ km} \times 5 \text{ km}$  region with 15 cm down-dip slip. The blue area is a  $10 \text{ km} \times 10 \text{ km}$  region with 5 cm down-dip slip. No slip occurs in the white area. Images (b)-(d) are the inverted fault slip distribution based on the optimal model with maximum likelihood estimated by the one-ellipse model (GICMo), the Laplacian smoothing and the von Karman smoothing (slipBERI). The dashed line in image (b)-(d) indicate the boundary of various slipping area in image (a).

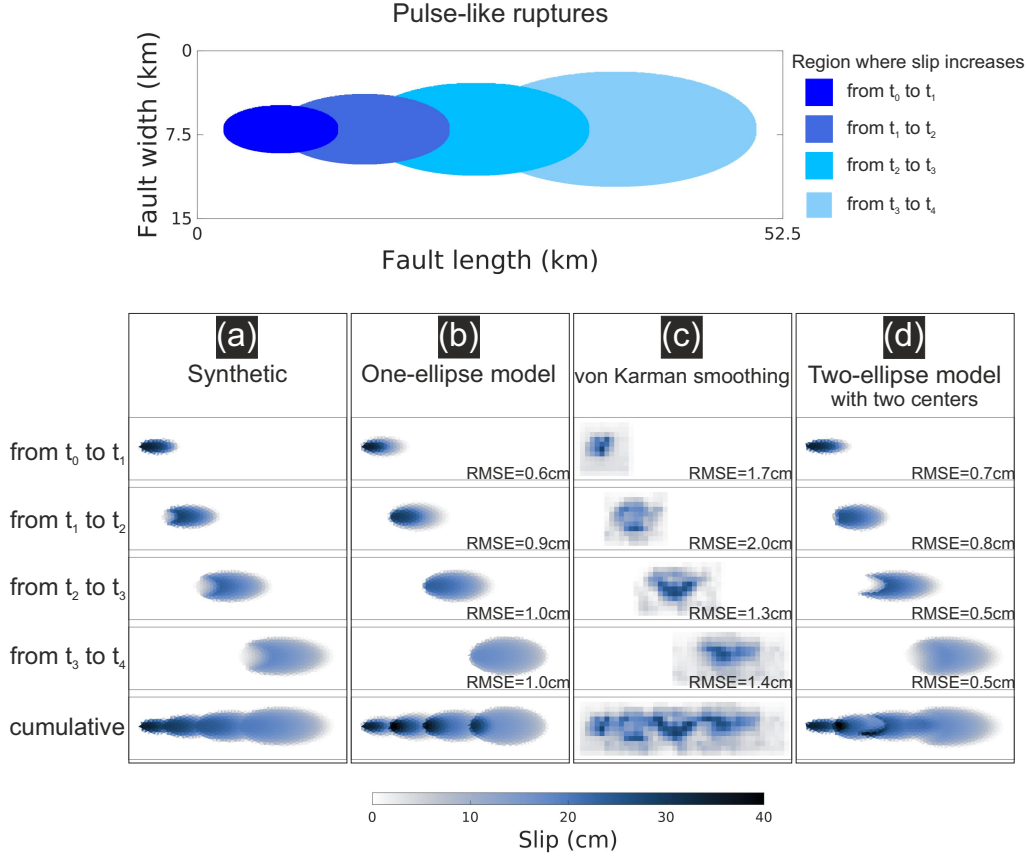


**Figure 3.** Synthetic and modelled fault slip distributions for synthetic case 2 (pulse-like ruptures). The top image is the conceptual diagram representing the growing cracks with the overlapping relationship. Images in column (a) show the synthetic slip increments. Images in columns (b)-(d) show the modelled slip distribution with various inversion methods: the one-ellipse model (b), the von Karman smoothing (c), and the two-ellipse model with different centres (d), and the RMSE of the slip residuals are shown at the bottom right.



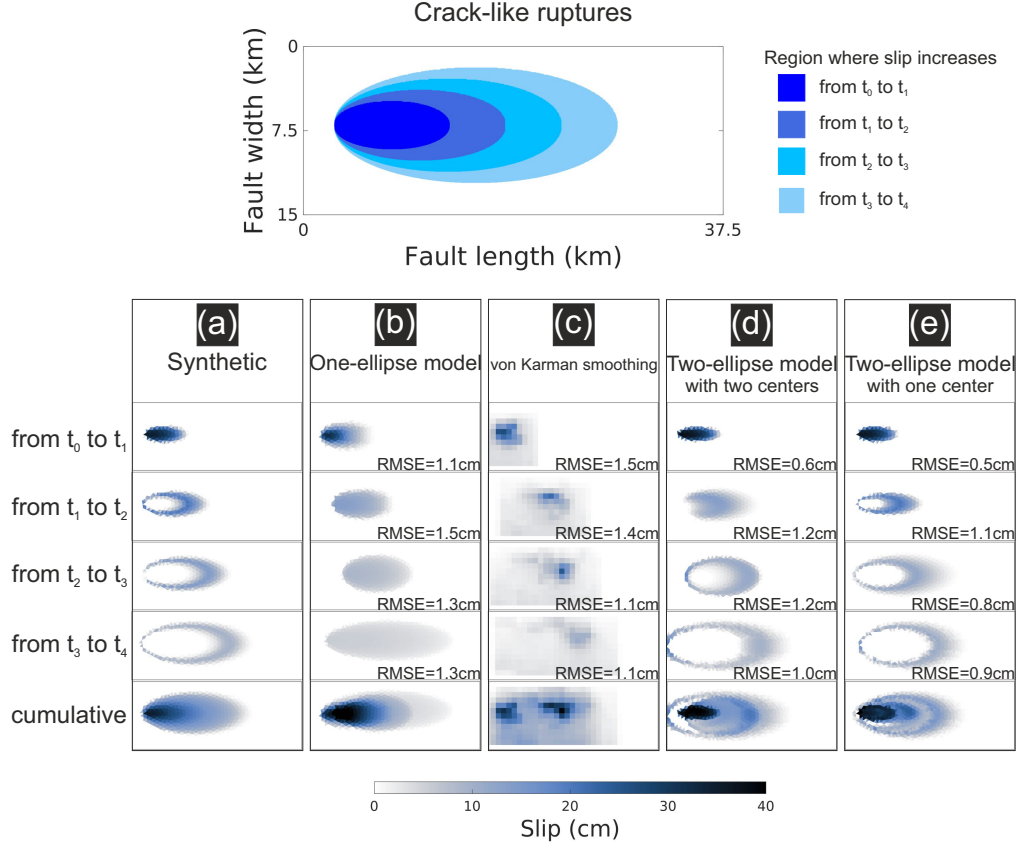


**Figure 4.** Synthetic and modelled fault slip distribution for synthetic case 2 (crack-like ruptures). The top image is the conceptual diagram presenting the growing cracks with the containing relationship. Images in column (a) show the synthetic slip increments. Images in columns (b)-(e) show the modelled slip distribution with various inversion methods: the one-ellipse model (b), the von Karman smoothing (c), the two-ellipse model with different centres (d) and with the same centre (e), and the RMSE of the slip residuals are shown at the bottom right.

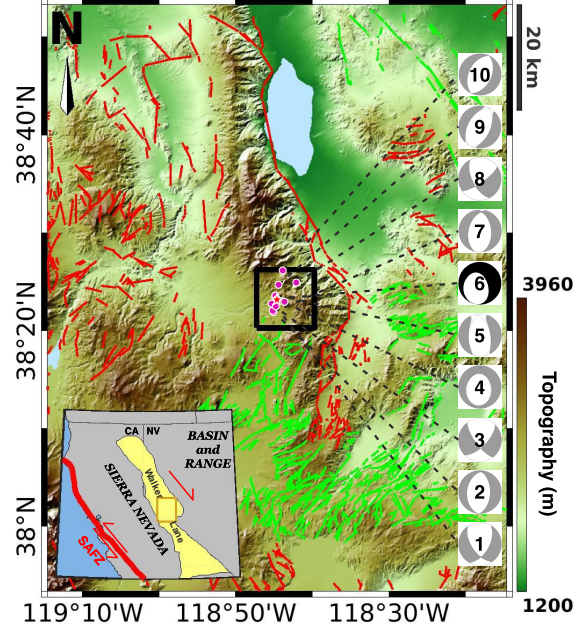


**Figure 5.** Tectonic settings for the 2011 Hawthorne seismic swarm. Image (a) shows the structural geologic environment of Walker Lane, located between the Sierra Nevada microplate and Basin and Range Province. It accommodates relative motion between the Pacific and North America. The brown rectangular box is the boundary of image (b), the central segment of Walker Lane. Image (b) shows the detailed tectonic settings for the 2011 Hawthorne seismic swarm, with topography as the base map. Normal and strike-slip faults are plotted as red and green lines. The beach balls on the right show the focal mechanism solutions provided by the Nevada Seismological Laboratory (Ichinose et al., 2003). Beach ball No.6 in black is the event with the largest magnitude, M4.6. Abbreviation: SAFZ, San Andreas Fault Zone.

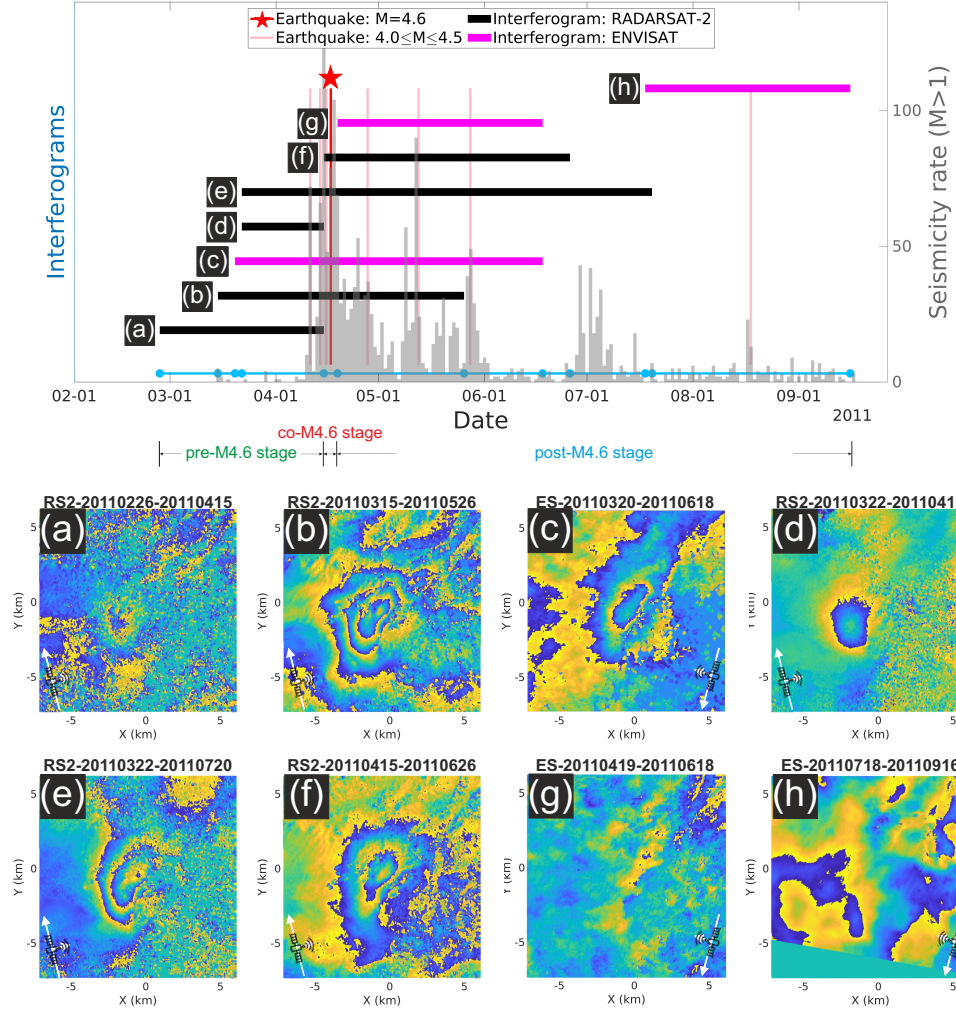


**Figure 6.** Surface displacement observations for the 2011 Hawthorne seismic swarm. In this research, the 2011 Hawthorne seismic swarm is divided into 3 stages with respect to the largest event, M4.6 on April 17 2011 (red star in the top image): pre-, co- and post-M4.6 event. The top image shows the time coverage of the interferograms (horizontal lines) over  $M \geq 4$  events (vertical lines). Out of 8 interferograms (a)-(h), 5 are from RADARSAT-2 (black lines) and 3 from ENVISAT (magenta lines). For the blue line at the bottom, dots infer the 11 dates for the image sensing time in the interferograms. Images (a)-(g) show the observed wrapped phases of the interferograms capturing the surface deformation of the seismic swarm, while no clear deformation signal is detectable in image (h). The spatial reference point is  $[38.3875^\circ\text{N}, 118.725^\circ\text{W}]$ .

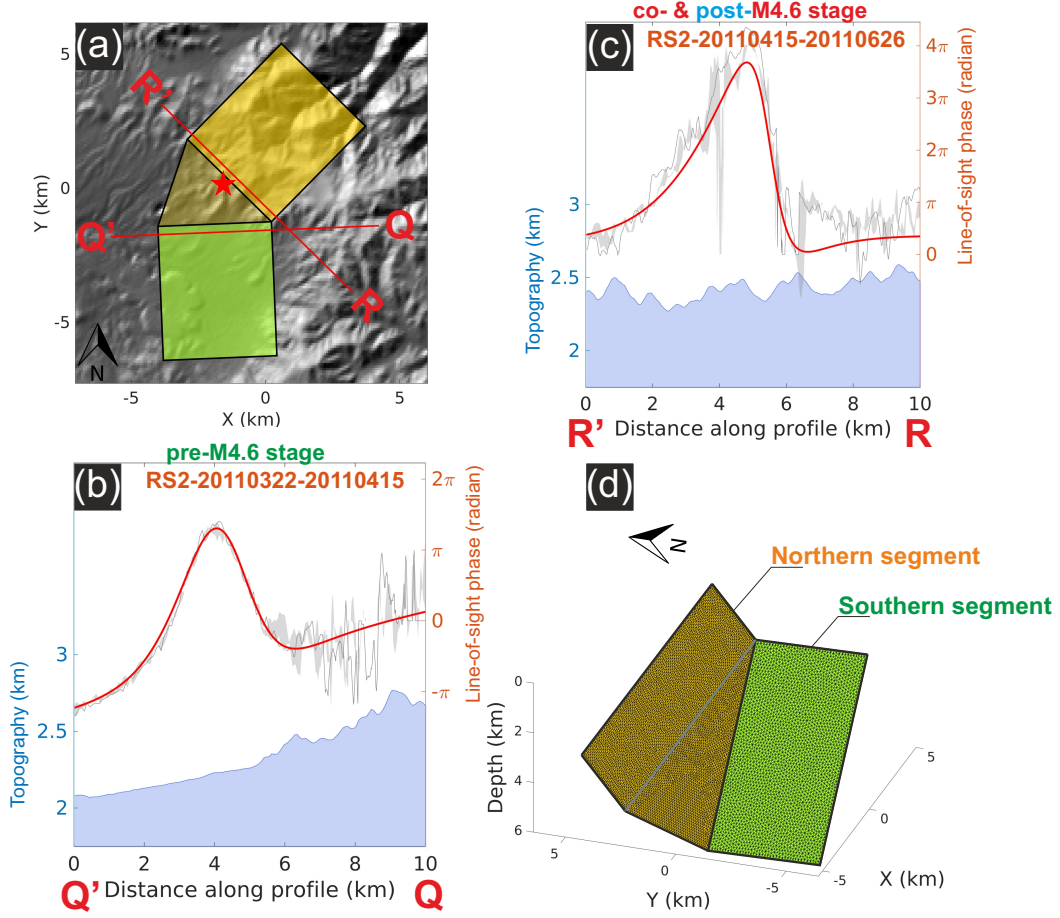


**Figure 7.** Fault geometry for the 2011 Hawthorne seismic swarm. Image (a) indicates the fault plane with uniform slip retrieved by WGBIS (Jiang & González, 2020) from the wrapped interferograms, and the modelled phase and phase residuals are shown in Figure S8. In image (a), the green rectangle indicates the southern subfault which is active during the pre-M4.6 stage, retrieved from RADARSAT-2 interferogram 2011/03/22-2011/04/15; yellow rectangle indicates the northern subfault which is active during the co- and post-M4.6 stages, retrieved from the RADARSAT-2 interferogram 2011/04/15-2011/06/26, and the yellow triangle indicates the joint fault connecting two rectangle subfaults. Profiles QQ' and RR' are perpendicular to two rectangle subfaults and the red star indicates the hypocentre of the M4.6 event. Images (b) and (c) show the observed and modelled phase along profiles QQ' and RR'. Image (d) shows the discretization of the fault geometry in image (a), where the triangular mesh is generated by FaultResampler (Barnhart & Lohman, 2010) and mesh2d (Engwirda, 2014).

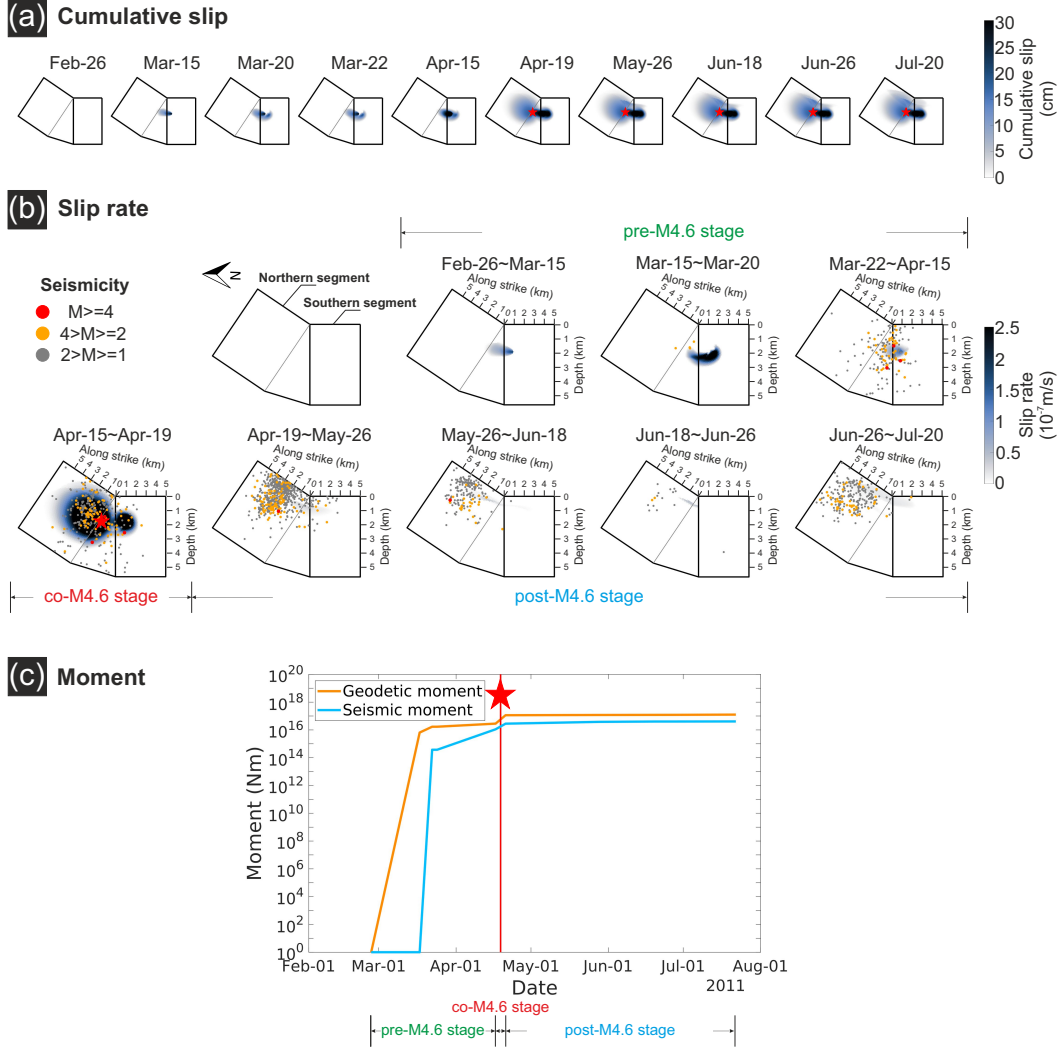


**Figure 8.** Slip evolution obtained from Time-GICMo inversion of pre-, co- and post-M4.6 stages during 2011 Hawthorne seismic swarm. Image (a) shows the accumulated slip at 10 dates, representing the acquisition time of images in Figures 6a to 6g. Image (b) presents the slip rate during the pre-, co- and post-M4.6 stages. In image (c), blue line shows the cumulative seismic moment based on the USGS earthquake catalog in the region  $[38.325^{\circ}\text{N} \sim 38.45^{\circ}\text{N}, 118.675^{\circ}\text{W} \sim 118.775^{\circ}\text{W}]$  (<https://earthquake.usgs.gov/earthquakes/search/>); orange line shows the cumulative geodetic moment, on the basis of estimated cumulative slip in image (a). A variable crustal shear modulus with depth is assumed based on the CRUST 1.0 model in the moment calculation.

# Supporting Information for "Aseismic Fault Slip during a Shallow Normal-Faulting Seismic Swarm Constrained Using a Physically-Informed Geodetic Inversion Method"

Yu Jiang<sup>1</sup>, Sergey V. Samsonov<sup>2</sup>, and Pablo J. González<sup>1,3</sup>

<sup>1</sup>COMET, Dept. Earth, Ocean and Ecological Sciences, School of Environmental Sciences, University of Liverpool, Liverpool, L69

3BX, United Kingdom.

<sup>2</sup>Canada centre for Mapping and Earth Observation, Natural Resources Canada, 560 Rochester Street, Ottawa, ON K1S5K2,

Canada.

<sup>3</sup>Department of Life and Earth Sciences, Instituto de Productos Naturales y Agrobiología (IPNA-CSIC), 38206 La Laguna,

Tenerife, Canary Islands, Spain.

## Contents of this file

1. Figures S1 to S10
2. Tables S1

**Introduction** This document contains supplementary figures and table. Figure S1 shows the observed and modelled InSAR phase for the synthetic case 1. Figures S2-S3 show the observed and modelled InSAR phase for synthetic case 2 (pulse-like ruptures). Figure S4-S5 show the observed and modelled InSAR phase for synthetic case 2 (crack-like ruptures). Figure S6 shows the wrapped and unwrapped InSAR phase for the descending ENVISAT

---

interferogram. Figure S7 shows the estimation of the covariance function from the non-deformed region. Figure S8 shows the inversion for two subfaults in the 2011 Hawthorne swarm, including the southern subfault in the pre-M4.6 stage, and the northern subfault during the co- and post-M4.6 stage. Figure S9 shows the modelled InSAR phases based on the fault geometry from nonlinear inversion (WGBIS). Figure S10 shows the degree of similarity between idealised one-ellipse crack model and published finite slip distribution datasets as a function of magnitudes. Table S1 summarised the parameters of slow slip listed in Section 5.2. For each event the table lists the event location, date, type and the reference from which the information was obtained.

## References

- Bletery, Q., & Nocquet, J. M. (2020). Slip bursts during coalescence of slow slip events in Cascadia. *Nature Communications*, 11(1), 1–6. doi: 10.1038/s41467-020-15494-4
- Cheloni, D., D’Agostino, N., Selvaggi, G., Avallone, A., Fornaro, G., Giuliani, R., ... Tizzani, P. (2017). Aseismic transient during the 2010-2014 seismic swarm: Evidence for longer recurrence of  $M \geq 6.5$  earthquakes in the Pollino gap (Southern Italy)? *Scientific Reports*, 7(1), 1–10. doi: 10.1038/s41598-017-00649-z
- De Barros, L., Cappa, F., Deschamps, A., & Dublanchet, P. (2020). Imbricated Aseismic Slip and Fluid Diffusion Drive a Seismic Swarm in the Corinth Gulf, Greece. *Geophysical Research Letters*, 47(9). doi: 10.1029/2020GL087142
- Guglielmi, Y., Cappa, F., Avouac, J. P., Henry, P., & Elsworth, D. (2015). Seismicity triggered by fluid injection-induced aseismic slip. *Science*, 348(6240), 1224–1226. doi: 10.1126/science.aab0476
- Hirose, H., & Obara, K. (2010). Recurrence behavior of short-term slow slip and corre-

- lated nonvolcanic tremor episodes in western Shikoku, southwest Japan. *Journal of Geophysical Research: Solid Earth*, 115(B6), 0–21. doi: 10.1029/2008JB006050
- Houston, H., Delbridge, B. G., Wech, A. G., & Creager, K. C. (2011). Rapid tremor reversals in Cascadia generated by a weakened plate interface. *Nature Geoscience*, 4(6), 404–409. doi: 10.1038/ngeo1157
- Hussain, E., Hooper, A., Wright, T. J., Walters, R. J., & Bekaert, D. P. (2016). Inter-seismic strain accumulation across the central North Anatolian Fault from iteratively unwrapped InSAR measurements. *Journal of Geophysical Research: Solid Earth*, 121(12), 9000–9019. doi: 10.1002/2016JB013108
- Jiang, Y., & González, P. J. (2020). Bayesian Inversion of Wrapped Satellite Interferometric Phase to Estimate Fault and Volcano Surface Ground Deformation Models. *Journal of Geophysical Research: Solid Earth*, 125(5). doi: 10.1029/2019JB018313
- Johanson, I. A., & Bürgmann, R. (2005). Creep and quakes on the northern transition zone of the San Andreas fault from GPS and InSAR data. *Geophysical Research Letters*, 32(14), 1–5. doi: 10.1029/2005GL023150
- Jolivet, R., Lasserre, C., Doin, M. P., Guillaso, S., Peltzer, G., Dailu, R., ... Xu, X. (2012). Shallow creep on the Haiyuan Fault (Gansu, China) revealed by SAR Interferometry. *Journal of Geophysical Research: Solid Earth*, 117(B6), 6401. doi: 10.1029/2011JB008732
- Khoshmanesh, M., Shirzaei, M., & Nadeau, R. M. (2015). Time-dependent model of aseismic slip on the central San Andreas Fault from InSAR time series and repeating earthquakes. *Journal of Geophysical Research: Solid Earth*, 120(9), 6658–6679. doi: 10.1002/2015JB012039



- Kyriakopoulos, C., Chini, M., Bignami, C., Stramondo, S., Ganas, A., Kolligri, M., & Moshou, A. (2013). Monthly migration of a tectonic seismic swarm detected by DInSAR: Southwest Peloponnese, Greece. *Geophysical Journal International*, *194*(3), 1302–1309. doi: 10.1093/gji/ggt196
- López-Comino, J. A., Stich, D., Morales, J., & Ferreira, A. M. (2016). Resolution of rupture directivity in weak events: 1-D versus 2-D source parameterizations for the 2011, Mw 4.6 and 5.2 Lorca earthquakes, Spain. *Journal of Geophysical Research: Solid Earth*, *121*(9), 6608–6626. doi: 10.1002/2016JB013227
- Mesimeri, M., & Karakostas, V. (2018). Repeating earthquakes in western Corinth Gulf (Greece): Implications for aseismic slip near locked faults. *Geophysical Journal International*, *215*(1), 659–676. doi: 10.1093/gji/ggy301
- Nadeau, R. M., & McEvilly, T. V. (1999). Fault slip rates at depth from recurrence intervals of repeating microearthquakes. *Science*, *285*(5428), 718–721. doi: 10.1126/science.285.5428.718
- Ozawa, S., Yarai, H., & Kobayashi, T. (2019). Recovery of the recurrence interval of Boso slow slip events in Japan. *Earth, Planets and Space*, *71*(1), 1–8. doi: 10.1186/s40623-019-1058-y
- Passarelli, L., Rivalta, E., Jónsson, S., Hensch, M., Metzger, S., Jakobsdóttir, S. S., ... Dahm, T. (2018). Scaling and spatial complementarity of tectonic earthquake swarms. *Earth and Planetary Science Letters*, *482*, 62–70. doi: 10.1016/j.epsl.2017.10.052
- Radiguet, M., Cotton, F., Vergnolle, M., Campillo, M., Valette, B., Kostoglodov, V., & Cotte, N. (2011). Spatial and temporal evolution of a long term slow slip event: the

2006 Guerrero Slow Slip Event. *Geophysical Journal International*, 184(2), 816–828.

doi: 10.1111/j.1365-246X.2010.04866.x

Rousset, B., Fu, Y., Bartlow, N., & Bürgmann, R. (2019). Weeks-Long and Years-Long Slow Slip and Tectonic Tremor Episodes on the South Central Alaska Megathrust. *Journal of Geophysical Research: Solid Earth*, 124(12), 13392–13403. doi: 10.1029/2019JB018724

Schmidt, D. A., Bürgmann, R., Nadeau, R. M., & D'Alessio, M. (2005). Distribution of aseismic slip rate on the Hayward fault inferred from seismic and geodetic data. *Journal of Geophysical Research: Solid Earth*, 110(B8), 1–15. doi: 10.1029/2004JB003397

Scott, C., Bunds, M., Shirzaei, M., & Toke, N. (2020). Creep Along the Central San Andreas Fault From Surface Fractures, Topographic Differencing, and InSAR. *Journal of Geophysical Research: Solid Earth*, 125(10), e2020JB019762. doi: 10.1029/2020JB019762

Song, X., Jiang, Y., Shan, X., Gong, W., & Qu, C. (2019). A Fine Velocity and Strain Rate Field of Present-Day Crustal Motion of the Northeastern Tibetan Plateau Inverted Jointly by InSAR and GPS. *Remote Sensing 2019, Vol. 11, Page 435*, 11(4), 435. doi: 10.3390/RS11040435

Turner, R. C., Nadeau, R. M., & Bürgmann, R. (2013). Aseismic slip and fault interaction from repeating earthquakes in the Loma Prieta aftershock zone. *Geophysical Research Letters*, 40(6), 1079–1083. doi: 10.1002/grl.50212

Wech, A. G., Creager, K. C., & Melbourne, T. I. (2009). Seismic and geodetic constraints on Cascadia slow slip. *Journal of Geophysical Research: Solid Earth*, 114(10). doi:

X - 6

:

10.1029/2008JB006090

June 17, 2022, 3:50am

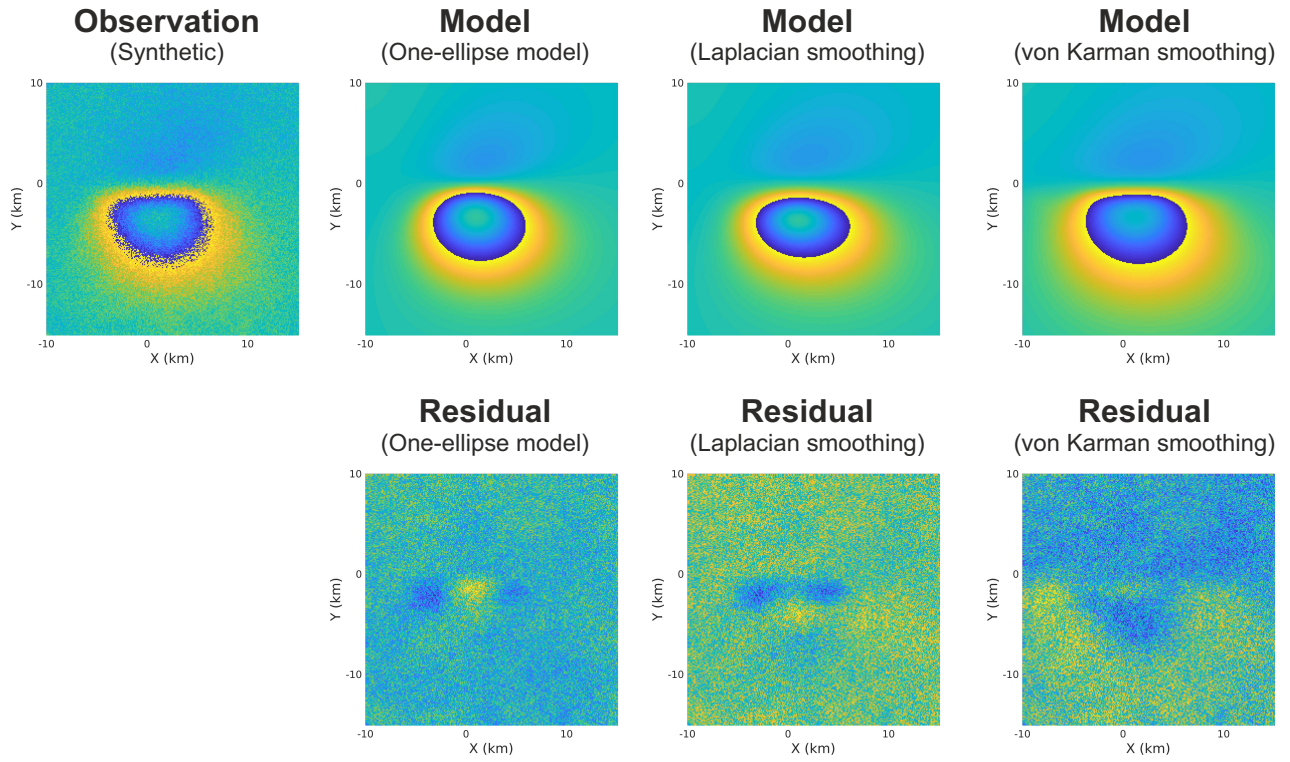


**Figure S1.** Synthetic and modelled InSAR phases for a synthetic case. The observed InSAR phase is forward calculated on the basis of the synthetic fault slip in Figure 2(a). The modelled InSAR phases are forward calculated on the basis of modelled slip distributions in Figure 2(b)-(c) estimated by the one-ellipse model and the laplacian smoothing. The bottom images show the residual phases.

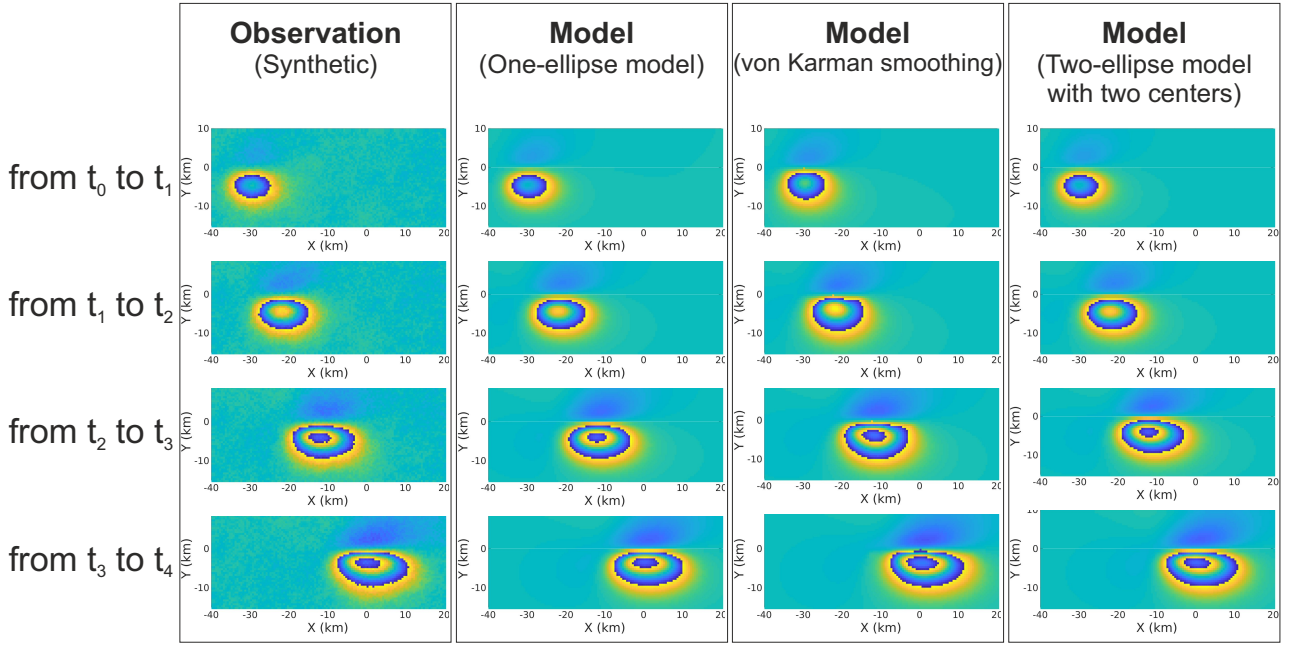


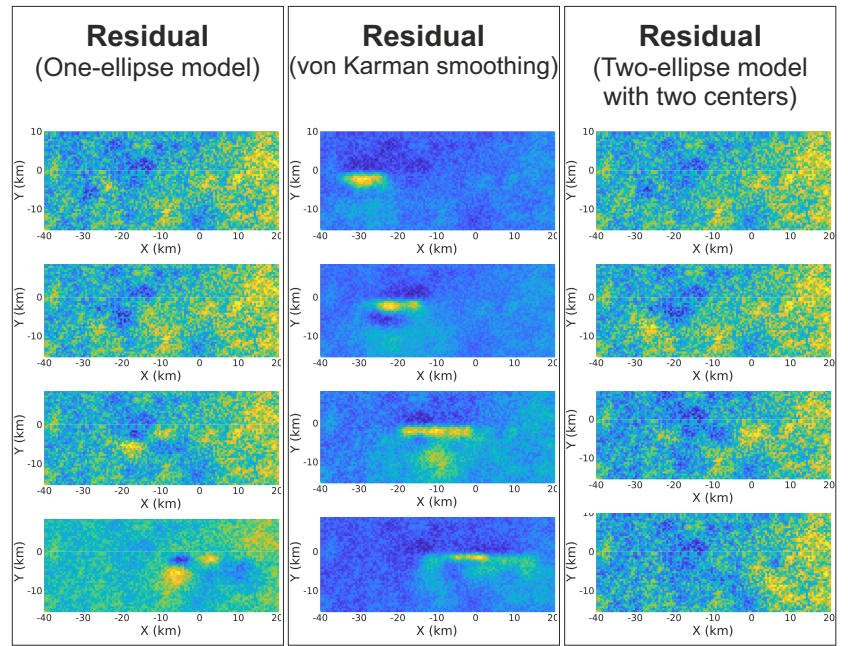
**Figure S2.** Synthetic and modelled InSAR phases for synthetic case 2 (pulse-like ruptures). The observed InSAR phase is forward calculated on the basis of the synthetic fault slip in Figure 3(a). The modelled InSAR phases are forward calculated on the basis of modelled slip distributions in Figure 3(b)-(d) with various methods: the one-ellipse model, the von Karman smoothing, and the two-ellipse model with different centres.

from  $t_0$  to  $t_1$

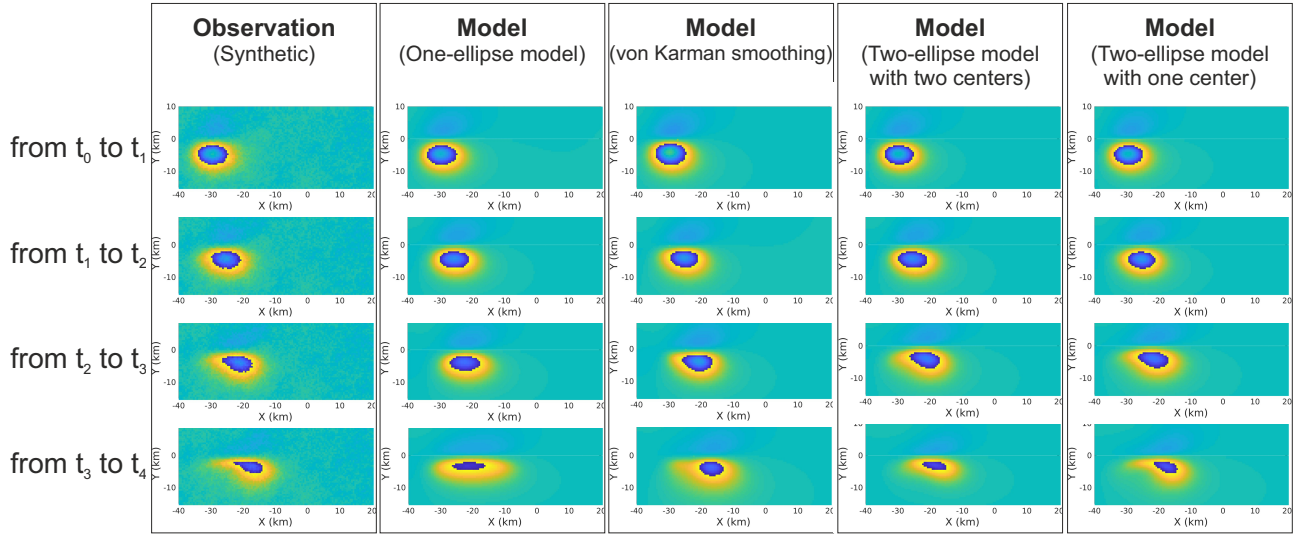
from  $t_1$  to  $t_2$

from  $t_2$  to  $t_3$

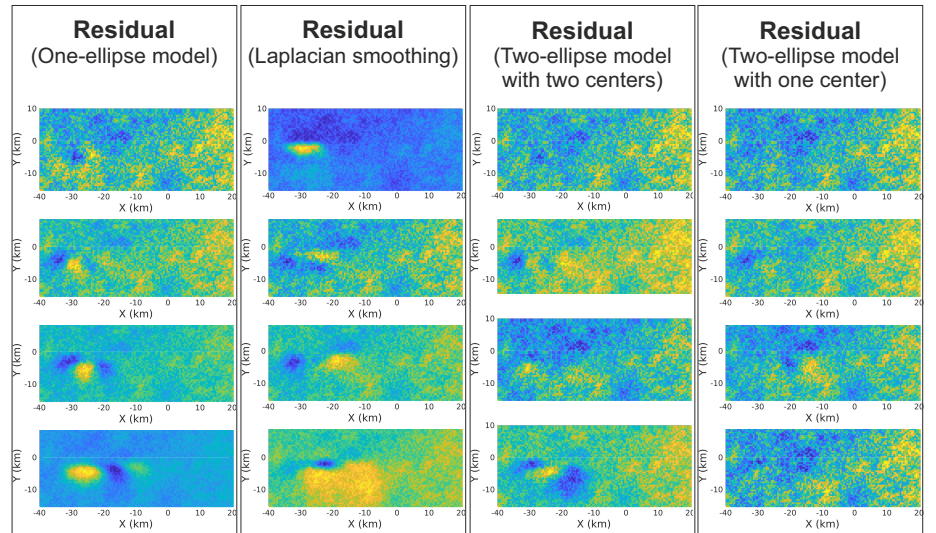
from  $t_3$  to  $t_4$



**Figure S3.** Residual InSAR phases for synthetic case 2 (pulse-like ruptures).



**Figure S4.** Synthetic and modelled InSAR phases for synthetic case 2 (crack-like ruptures). The observed InSAR phase is forward calculated on the basis of the synthetic fault slip in Figure 4(a). The modelled InSAR phases are forward calculated on the basis of modelled slip distributions in Figure 4(b)-(e) with various methods: the one-ellipse model, the von Karman smoothing, and the two-ellipse model with different centres and with the same centre.

from  $t_0$  to  $t_1$ from  $t_1$  to  $t_2$ from  $t_2$  to  $t_3$ from  $t_3$  to  $t_4$ 

**Figure S5.** Residual InSAR phases for synthetic case 2 (crack-like ruptures).



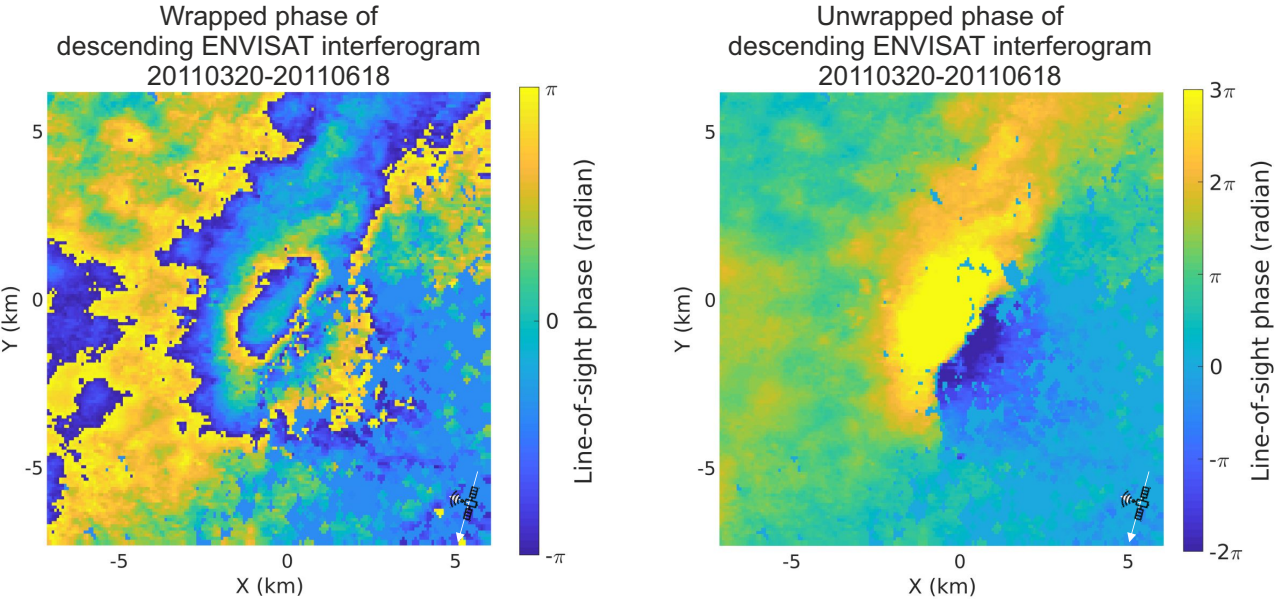


**Figure S6.** Wrapped and unwrapped phase in the descending ENVISAT interferogram 2011/03/20-2011/06/18.

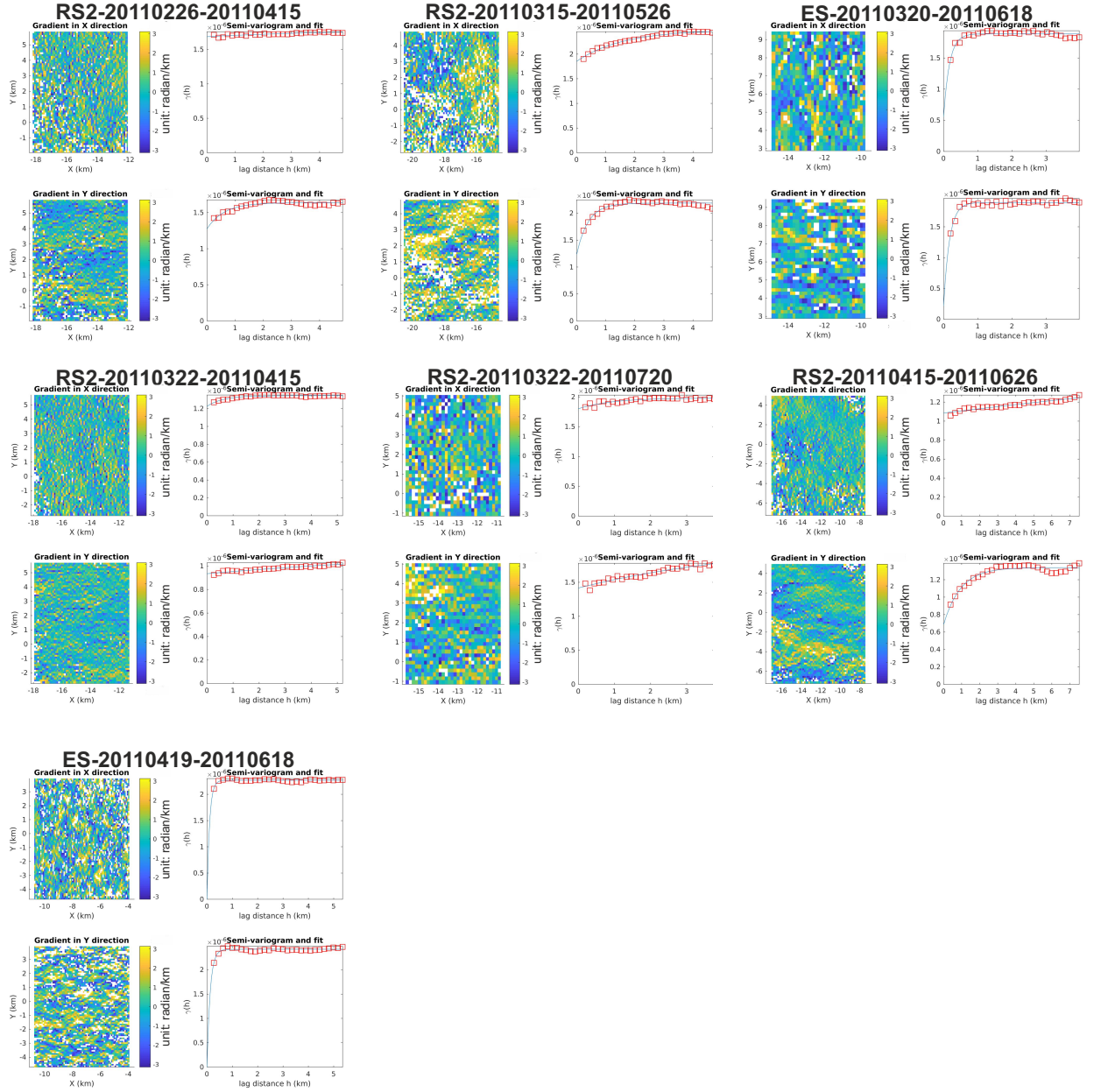


**Figure S7.** Covariance function estimation from the phase in the nondeformed region of the interferograms used in the 2011 Hawthorne seismic swarm. The chosen region for covariance estimation is the undeformed region. For each panel, images on the left are the downsampled phase gradients in X-direction and Y-direction; images on the right side show the experimental (rectangular) and theoretical (solid line) semivariograms are shown for phase gradients in X-direction and Y-direction, estimating from the downsampled phase gradients according to equation 9 in Jiang and González (2020).

June 17, 2022, 3:50am

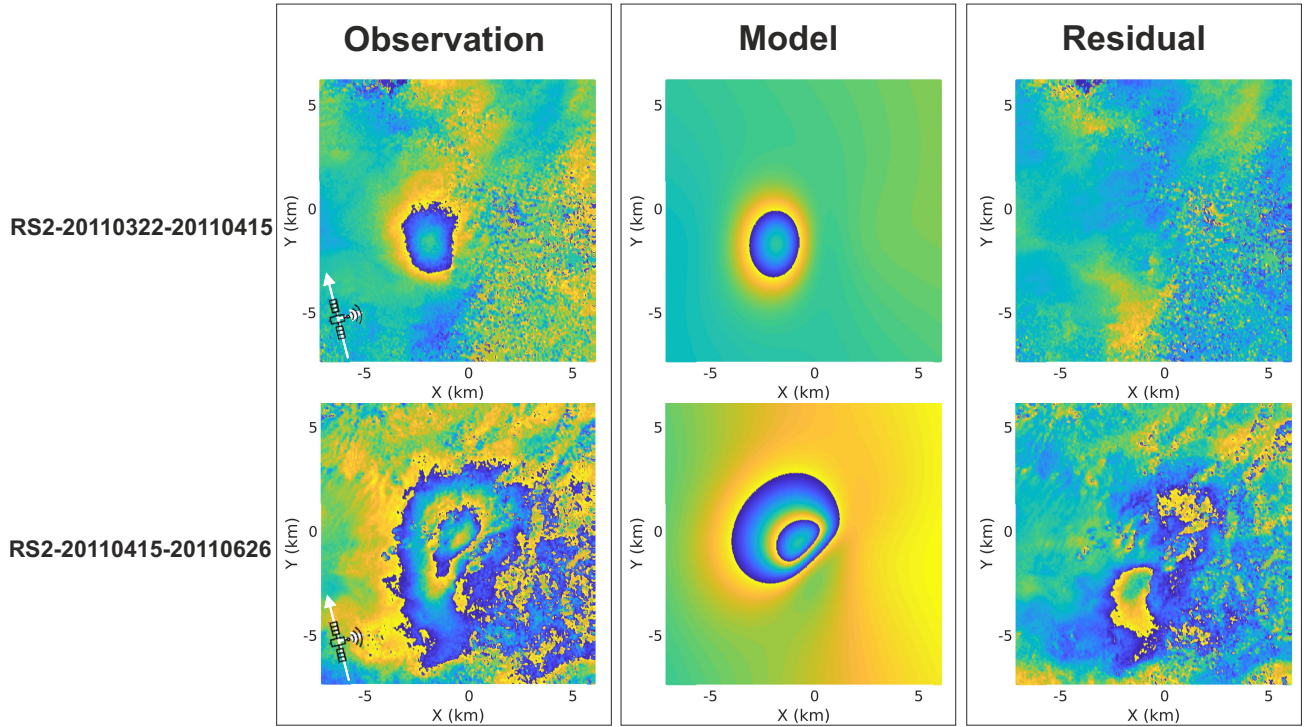


**Figure S8.** Observed and modelled InSAR displacements with WGBIS. Images at the top row show the observed, modelled and residual phases for ascending RADARSAT-2 interferogram 2011/03/22-2011/04/15, covering the pre-M4.6 stage of the 2011 Hawthorne swarm. Images at the bottom row show the observed, modelled and residual phases for ascending RADARSAT-2 interferogram 2011/04/15-2011/06/26, covering the co- and post-M4.6 stage of the 2011 Hawthorne swarm.



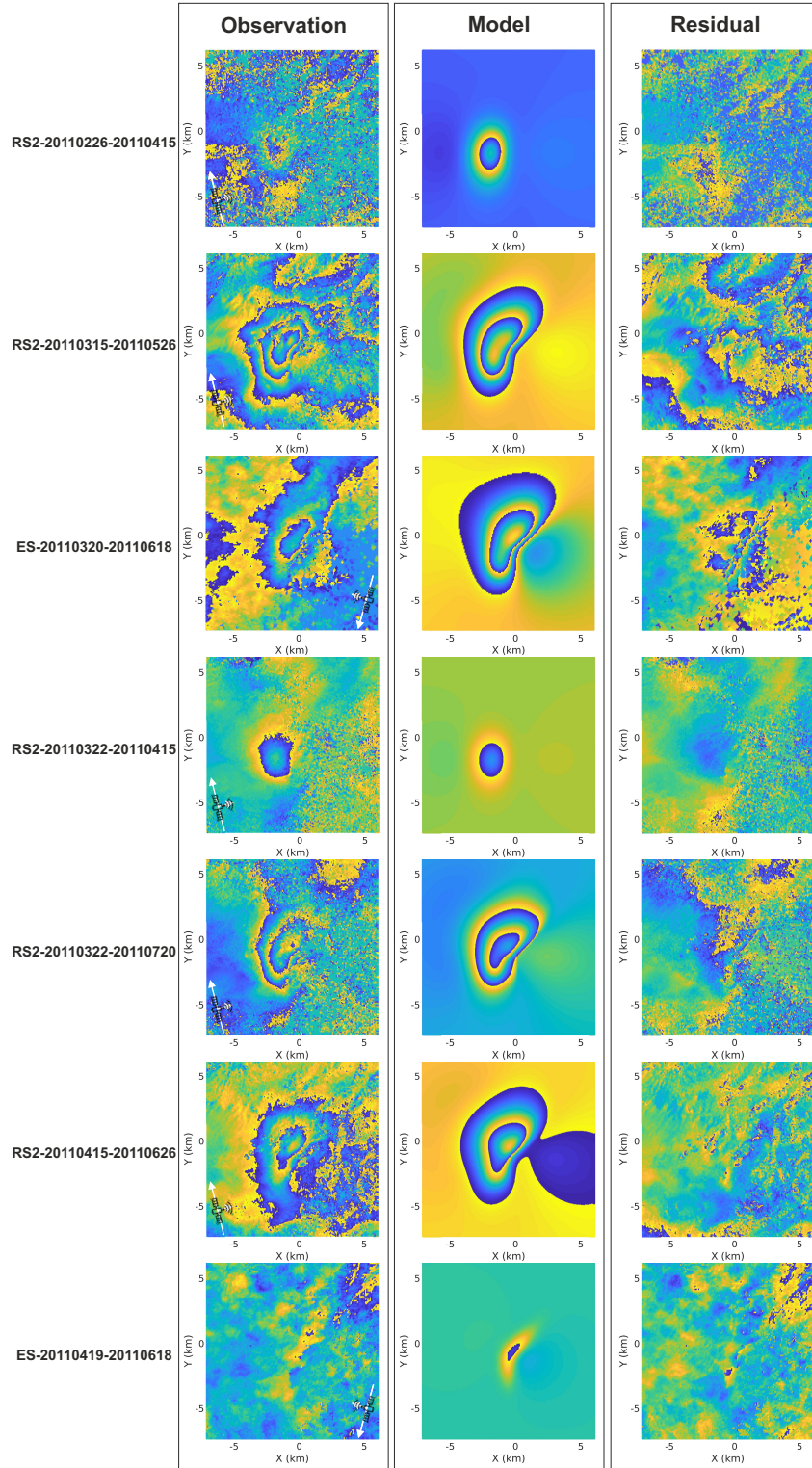


**Figure S9.** Observed and modelled InSAR displacements of the 2011 Hawthorne swarm by using the discretized fault geometry retrieved from WGBIS. The modelled phases are forward calculated on the basis of the modelled slip distributions in Figure 8(a) and discretized fault geometry in Figure 7(d).

June 17, 2022, 3:50am

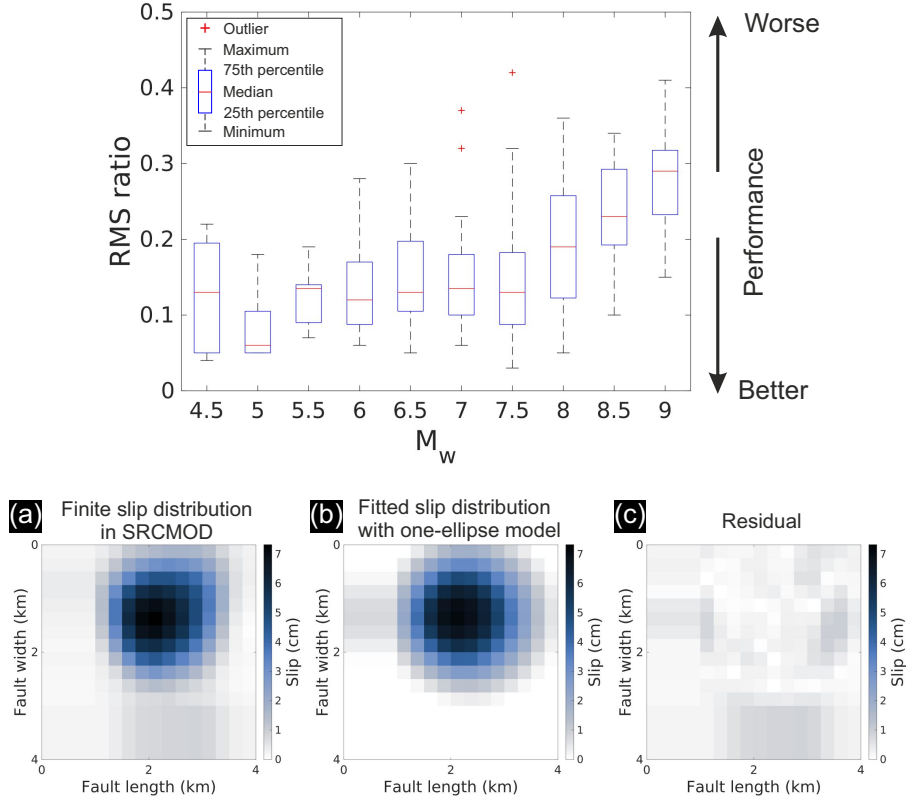


**Figure S10.** This figure shows the degree of similarity between idealised one-ellipse crack model and published finite slip distribution datasets as a function of magnitudes. A one-ellipse crack model is used to approximate the finite slip distributions in SRCMOD for each dataset containing 25 fault patches or more. We obtain a best fitting model for each selected dataset. We estimate the misfit between the best fitting crack model and SRCMOD estimated fault slips as the RMSE. Top image presents the ratio between RMSE and peak slip for each case in the SRCMOD dataset. Lower values of the ratio indicate better agreement. Bottom images present an example for comparison of a SRCMOD event (2011  $M_w$  4.6 Lorca earthquakes, Spain, López-Comino et al. (2016)) and its best-fitting ellipse model.

**Table S1.** Parameters of slow slip phenomena considered in this study

Name	Type	Value	Source location and date	(Reference)
Peak slip rate (cm/day)	SSE	0.27	[124°W, 49°N], Cascadia subduction zone, 2013	(Bletery & Nocquet, 2020)
		0.3	[149°W, 62°N], Central Alaska Megathrust, 2010	(Rousset et al., 2019)
		0.6-1.1	[132.5°E, 33.5°N], Western Shikoku, Japan, 2002-2007	(Hirose & Obara, 2010)
		1.1-2.8	[141°E, 35°N], Boso peninsula, Japan, 1996-2018	(Ozawa et al., 2019)
	Seismic swarm	0.26	[22°E, 37.24°N], Peloponnese peninsula, Greece, 2011	(Kyriakopoulos et al., 2013)
	Fluid injection experiments	35	France, ?	(Guglielmi et al., 2015)
	Fault creep	0.001	[122.25°W, 37.5°N], Hayward fault, USA, 1992-2000	(Schmidt et al., 2005)
		0.001	[105°E, 36.5°N], Haiyuan fault, China, 2003-2010	(Jolivet et al., 2012); (Song et al., 2019)
		0.002	[32.5°E, 40.75°N], North Anatolia fault, Turkey, 2003-2010	(Hussain et al., 2016)
		0.005	[121.4°W, 36.8°N], San Andreas fault, USA, 2001-2003	(Johanson & Bürgmann, 2005)
		0.008	[121°W, 36.2°N], Central segment of San Andreas fault, USA, 2003-2011	(Khoshmanesh et al., 2015)
		0.007	[121°W, 36.4°N], Central segment of San Andreas fault, USA, 2012-2020	(Scott et al., 2020)
Average rate of slip increment (cm/day)	SSE	0.03-0.14	[100°W, 18°N], Mexican subduction zone, 2006	(Radiguet et al., 2011)
	Seismic swarm	0.1	[16°E, 39.9°N], Pollino gap, Southern Italy, 2010-2014	(Cheloni et al., 2017)
	Repeating earthquakes	0.01	[116.7°W, 36.7°N], San Andreas fault, USA, 1994	(Nadeau & McEvilly, 1999)
		0.003	[121.6°W, 36.8°N], San Andreas fault, USA, 2003-2006	(Turner et al., 2013)
		0.0006	[22°E, 38.4°N], Corinth Gulf, Greece, 2008-2014	(Mesimeri & Karakostas, 2018)
Migration velocity (km/day)	SSE	~10	[132.5°E, 33.5°N], Western Shikoku, Japan, 2002-2007	(Hirose & Obara, 2010)
	ETS	~10	[123.5°W, 48.5°N], Cascadia subduction zone, 2004-2008	(Wech et al., 2009)
	RTR	160-400	[123°W, 48°N], Cascadia subduction zone, 2004-2009	(Houston et al., 2011)
	Seismic swarm	0.5-14	[18.6°W, 66.3°N], North Iceland, 1997-2015	(Passarelli et al., 2018)
		2-10	[22°E, 38.4°N], Corinth Gulf, Greece, 2015	(De Barros et al., 2020)